Data-Driven Characterization of Micro-structural Shape and Topology in Engineering Materials

Kuang Kuang

Thesis submitted to the Faculty of the

Virginia Polytechnic Institute and State University

in partial fulfillment of the requirements for the degree of

Master of Science

in

Mechanical Engineering

Pinar Acar, Chair

Jie Chen

Robert West

May 8, 2025

Blacksburg, Virginia

Keywords: Microstructure, Image Processing, Shape and Topology Quantification, Engineering Materials, etc.

Data-Driven Characterization of Micro-structural Shape and Topology in Engineering Materials

Kuang Kuang

(ABSTRACT)

This thesis presents a data-driven framework for the quantitative characterization of micro-structural shape and topology in engineering materials, integrating invariant geometric descriptors and statistical dimensionality reduction techniques. Specifically, Hu moments, Principal Eigenvalue Moment (PEM), and Principal Component Analysis (PCA) are applied to a diverse dataset comprising experimental images of Titanium-Aluminum alloys and Inconel 718 superalloy, computationally designed meta-materials including unit cells and spinodoids, and synthetic microstructures generated via deep learning models such as Progressive Generative Adversarial Network (PGAN) and Denoising Diffusion Probabilistic Models (DDPM). Both Hu moments and PEM portray a high degree of invariance to rotation and scaling, showing considerable effectiveness in capturing morphologic features like grain size, ellipticity, and asymmetry. PCA provides a complementary perspective by revealing global variance patterns in pixel intensity distributions, although it is sensitive to rotation and color information. The result reflects that synthetic images generated from DDPM closely mimic real microstructure data in terms of both shape and texture, whereas images from the PGAN model align better with color-based PCA. The framework supports reproducible and scalable quantification of microstructures, which aids materials informatics, classification, and computational materials design.

Data-Driven Characterization of Micro-structural Shape and Topology in Engineering Materials

Kuang Kuang

(GENERAL AUDIENCE ABSTRACT)

Materials employed in aerospace and other engineering fields need to possess a unique combination of properties - being exceptionally strong, lightweight, and resistant to harsh environments. These attributes depend not only on the constituents of the material, but also on the internal structure, known as the *microstructure*, which demonstrates geometric features that are shaped and ordered. This research proposes novel computational methods for the quantification and comparison of microstructures. It seeks to improve our understanding of the relationship between microstructure morphology and material performance by applying image processing techniques and sophisticated mathematical algorithms to images of various metals and synthetic materials. The study uses a mix of real materials (like Titanium-Aluminum and Nickel alloys) and artificially generated materials with machine learning methods. Through pattern comparison, the work accelerates evaluation processes for new materials and enables the development of materials designed with enhanced safety, efficiency, and adaptability for emerging technologies.

Contents

List of Figures

List of Tables

List of Abbreviations

$\bar{x}, \bar{y}$	centroids of the image
η_{pq}	normalized central moments
λ_k	eigenvalues
$\lambda_{1/2}$	principal eigenvalue moments
μ	mean vector
μ_{pq}	central moments
ϕ_i	Hu moments
$\tilde{X}$	centered data matrix
C	covariance matrix
$I(x, y)$	intensity of each pixel
M_{pq}	raw moments
p, q	moment orders
v_k	eigenvectors
W	matrix of selected eigenvectors
X	data matrix
X_{proj}	projected data

CT X-ray computed tomography

DDPM Denoising Diffusion Probabilistic Models

EBSD electron backscatter diffraction

FIB-SEM focused ion beam scanning electron microscopy

GRF Gaussian Random Fields

IPF Inverse Pole Figure

PC principal component

PCA Principal Component Analysis

PEM Principal Eigenvalue Moment

PGAN Progressive Generative Adversarial Network

RGB Red-Green-Blue

RVE representative volume element

Ti-Al Titanium-Aluminum alloys

Chapter 1

Introduction

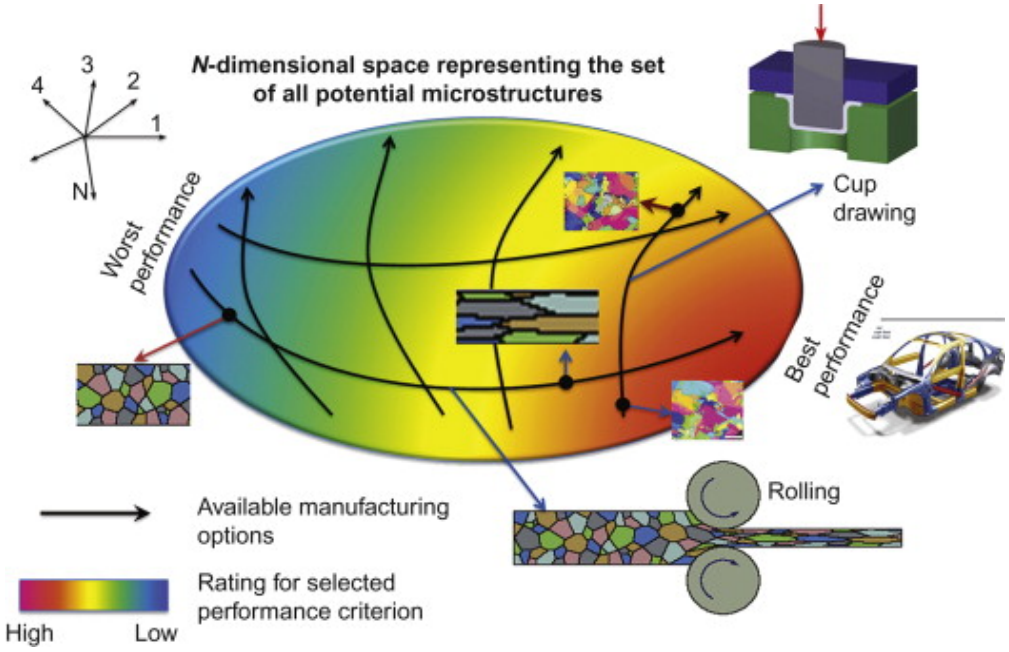

Figure 1.1: Schematic of the High-Dimensional Microstructure Space [20]

1.1 Role of Microstructures in Material Performance

Microstructure is the proper arrangement of a material which includes phases, grains, and defects in a scalable nanometer to micrometer range [19]. Its importance is in bridging the gap between a material's processing history and its mechanics, thermodynamics, and chemical attributes on a macro level. In most structural engineering materials, micro-structural features like grain size, shape, orientation, and topology have a significant impact on strength,

ductility, fatigue life, corrosion resistance, and overall performance [19]. Therefore, in high-performance materials integrated with aerospace, biomedicine, energy, and transportation, predicting material behavior becomes vital with the control and design of the features of the underlying microstructures.

1.2 Challenges in Traditional Microstructure Quantification

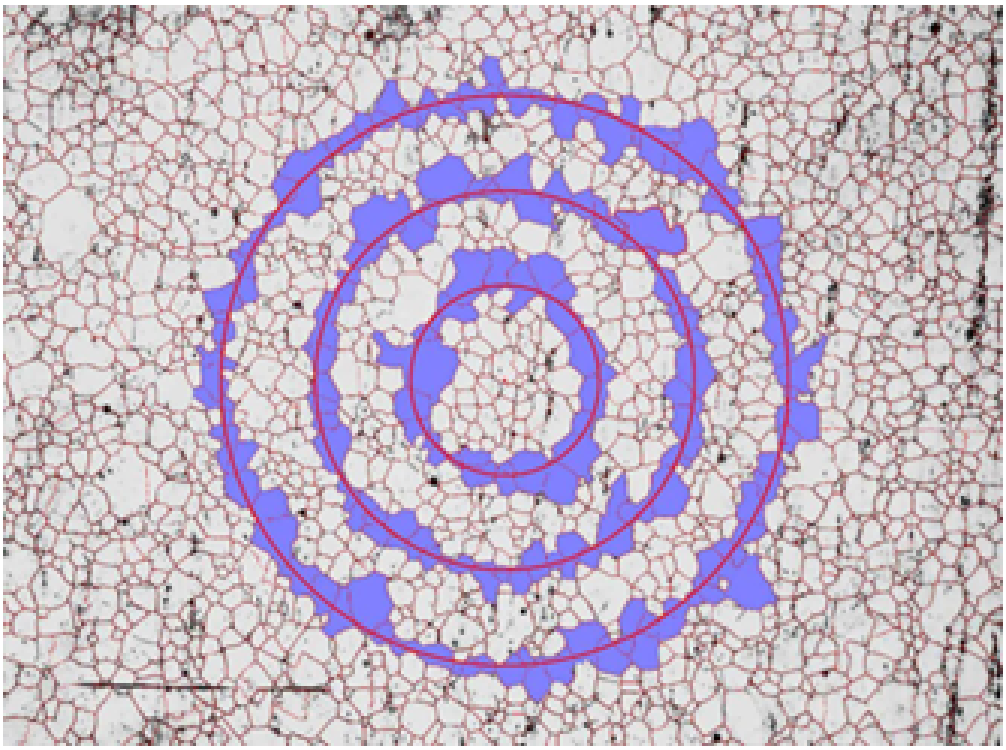

Figure 1.2: Grain Size Calculation using Intercept Technique [10]

Traditional methods used for microstructure quantification utilize qualitative or semi-quantitative approaches like manual labeling, visual inspection, or basic arithmetic calculations like average grain size and aspect ratio [2, 6, 10, 32]. Furthermore, the comparison of datasets from different material systems or with varying processing parameters is complicated by

differences in image capture quality, orientation, imaging scale, and resolution. Because there are no standardized, quantifiable benchmarks, it is impossible to systematically relate micro-structural features to functional attributes. This also stagnates advancement in the design and discovery of materials.

To address these challenges, this study proposes a quantitative approach to capture the morphological features of microstructures of different materials.

1.3 Proposed Metrics for Micro-structural Shape and Topology Quantification

This study addresses the quantification of microstructural morphology by developing a novel data-driven framework that integrates image-based shape description and dimension reduction algorithms to capture micro-structural shape and topology in a reproducible and scalable manner. The methodology is based on three main techniques: Hu moments, Principal Eigenvalue Moment (PEM), and Principal Component Analysis (PCA).

1.3.1 Hu Moments and Principal Eigenvalue Moments (PEM)

Hu moments are a specific set of seven geometric image moments which are invariant to rotation, translation, or even image scaling [13]. These descriptors form an effective, concisely-framed representation of shape that is useful for defining grain boundaries, porosity patterns, and other morphological attributes in micro-structural images [30]. The first and second Hu moments are the most critical descriptors, as they assist in the identification of critical features such as the grain shape formation as a result of the processing-induced micro-structural variations. Incorporating Hu moments, Principal Eigenvalue Moment (PEM) is proposed as

a scalar metric that combines the first and second Hu moments to represent overall shape complexity [31]. PEM enhances shape descriptors by integrating them into a single number, thus streamlining comparison and clustering of distinct micro-structures. With high robustness and invariant properties, PEM serves as an efficient estimator of summarizing micro-structural morphology in large-scale datasets that require condensed metrics for effective computation and visualization. Therefore, Hu moments together with PEM provide a powerful combination of shape-based metrics.

1.3.2 Principal Component Analysis (PCA)

Principal Component Analysis (PCA) is a technique in statistics used to reduce the dimensionality of a dataset while retaining as much variance as possible, by transforming the data into a new set of variables which are orthogonal to each other, termed as principal components [3]. In the context of image analysis, PCA transforms the pixel intensity distributions into components that capture the directions of maximum variance, facilitating visual comparison and clustering of large microstructure datasets. Unlike Hu moments and PEM, PCA is sensitive to the arrangement of an image and able to incorporate color (Red-Green-Blue (RGB) channels) information, thus serving as an additional and alternative method for micro-structural characterization.

1.4 Contributions

This study introduces advanced, data-driven metrics for characterizing micro-structural shape and topology in both experimental and synthetic material datasets. The framework is applied to a diverse range of materials, including Titanium-Aluminum alloys, Inconel 718

superalloy, computationally designed unit cell meta-materials and spinodoids, as well as the microstructures generated by deep learning models. The research shows that Hu moments and PEM develop shape descriptors that are rotation-invariant while PCA captures the variance pattern globally. Collectively, they allow an in-depth and quantitative analysis of microstructures in different materials and under different processing conditions. Such analysis helps in devising better tools for materials informatics and aids in designing advanced materials with performance attributes tailored to the requirements.

Chapter 2

Methodology

This chapter introduces the approaches and materials used to classify the shapes and topologies of microstructures. It is divided into the following subsections: "Microstructure Quantification using Data-Driven Metrics," where the mathematical tools such as Hu moments, Principal Eigenvalue Moments (PEM), and Principal Component Analysis (PCA) are discussed; and "Materials and Datasets," which presents the materials: Titanium-Aluminum alloys, Inconel-718, Unit-Cells and Spinodoids.

2.1 Microstructure Quantification using Data-Driven Metrics

2.1.1 Hu Moments and Principal Eigenvalue Moment (PEM)

A collection of geometric properties that are invariant to translation, scale, and rotation is referred to as Hu moments [13]. These are particularly useful when analyzing the shape of objects in the image processing field. These were first proposed by Hu in 1962 in his classical work 'Visual Pattern Recognition by Moment Invariants' and have since been used for numerous pattern recognition applications [16]. In the proposed research, Hu moments are calculated for the shape features of micro-structural elements such as grain shapes to

leverage their consistent classification irrespective of changes in imaging conditions.

In order to calculate Hu moments of an image, central moments need to be first obtained from Equation 2.1 [16]. Here, x and y refer to the position of each pixel, which starts from the top left (e.g., pixel at the top left will have both x and y equal to 0). In this representation, p and q are positive integers that refer to the moment order in x and y directions, respectively, and $I(x, y)$ represents the intensity of each pixel (from 0 to 255).

$$\mu_{pq} = \sum_{x} \sum_{y} (x - \bar{x})^p (y - \bar{y})^q I(x, y) \tag{2.1}$$

$$\bar{x} = \frac{M_{10}}{M_{00}}, \quad \bar{y} = \frac{M_{01}}{M_{00}} \tag{2.2}$$

$$M_{pq} = \sum_{x} \sum_{y} x^p y^q I(x, y) \tag{2.3}$$

In Equations 2.1 and 2.2, $\bar{x}$ and $\bar{y}$ are centroids of the image which can be derived using raw moments shown in Equation 2.3, where M_{00} represents the sum of pixel intensities in the region; M_{10} represents the sum of x-coordinates multiplied by pixel intensities; M_{01} represents the sum of y-coordinates multiplied by pixel intensities. The central moments are then normalized using Equation 2.4, which ensures that the moments do not change with different image sizes. The seven Hu moments can then be derived from the combination of normalized central moments as shown in Equation 2.5. For a better visualization, only the first and second Hu moments are plotted for each image. Moreover, since Hu moments are only focused on the shape and topology information, each image is transferred into grayscale before calculation. The formulation for the seven Hu moments (ϕ_i with $i = 1, 2, ..., 7$) is given next [31]:

$$\eta_{pq} = \frac{\mu_{pq}}{\mu_{00}^{1+\frac{p+q}{2}}} \tag{2.4}$$

$$\phi_1 = \eta_{20} + \eta_{02} \tag{2.5a}$$

$$\phi_2 = (\eta_{20} - \eta_{02})^2 + 4\eta_{11}^2 \tag{2.5b}$$

$$\phi_3 = (\eta_{30} - 3\eta_{12})^2 + (3\eta_{21} - \eta_{03})^2 \tag{2.5c}$$

$$\phi_4 = (\eta_{30} + \eta_{12})^2 + (\eta_{21} + \eta_{03})^2 \tag{2.5d}$$

$$\begin{aligned}\phi_5 = {} & (\eta_{30} - 3\eta_{12})(\eta_{30} + \eta_{12})[(\eta_{30} + \eta_{12})^2 - 3(\eta_{21} + \eta_{03})^2] \\ & + (\eta_{21} - \eta_{03})(\eta_{21} + \eta_{03})[3(\eta_{30} + \eta_{12})^2 - (\eta_{21} + \eta_{03})^2]\end{aligned} \tag{2.5e}$$

$$\phi_6 = (\eta_{20} - \eta_{02})[(\eta_{30} + \eta_{12})^2 - (\eta_{21} + \eta_{03})^2] + 4\eta_{11}(\eta_{30} + \eta_{12})(\eta_{21} + \eta_{03}) \tag{2.5f}$$

$$\begin{aligned}\phi_7 = {} & (3\eta_{21} - \eta_{03})(\eta_{30} + \eta_{12})[(\eta_{30} + \eta_{12})^2 - 3(\eta_{21} + \eta_{03})^2] \\ & - (\eta_{30} - 3\eta_{12})(\eta_{21} + \eta_{03})[3(\eta_{30} + \eta_{12})^2 - (\eta_{21} + \eta_{03})^2]\end{aligned} \tag{2.5g}$$

After computing the first and second Hu moments of an image, the principal eigenvalue moments (PEM) can be derived from them as shown in Equation 2.6. As a combination of the first and second Hu moments, principal eigenvalue moments are also invariant to translation, rotation, and scale, making them effective for quantifying the shapes (e.g., grain shapes) of microstructures. In addition to Hu moments, PEM consolidates multiple shape features into one metric, which makes the comparison and interpretation of microstructural data easier. It aids in visualization and clustering through reduced dimensionality seen in the analyses of metallic microstructures (Section 3.1). The PEM is formulated next.

$$\lambda_{1/2} = \frac{\phi_1 \pm \sqrt{\phi_2}}{2} \tag{2.6}$$

2.1.2 Principal Component Analysis (PCA)

Principal Component Analysis (PCA) is a technique that reduces the dimensionality of data by transforming a large set of variables into a smaller set of uncorrelated variables known as principal components, while retaining a maximum possible proportion of the original data's variability [3]. The term, PCA, was first described by Karl Pearson in 1901 in his published work "On Lines and Planes of Closest Fit to Systems of Points in Space" in Philosophical Magazine [28]. It was primarily aimed at simplifying complex datasets within statistics; PCA originated in an era where there was an increased focus on multivariate analysis. Its uses broadened over time, especially in image processing, materials science, and it became foundational in dealing with vast amounts of data, for example, in modeling the microstructures of engineering materials [8, 12, 21, 23, 27, 29, 35].

To implement PCA on a group of images, each image is first converted into a 1-D vector. For example, a 50×50 grayscale image is flattened into a $1 \times 2,500$ vector; for a same size but color image, which in this study a three channel RGB image. Thus, it becomes a $1 \times 7,500$ vector ($50 \times 50 \times 3$). The way to convert a grayscale image into a 1-D vector is to concatenate each row consecutively from top to bottom. Similarly, to obtain a 1-D vector from a color image, where each pixel contains three intensity values corresponding to the RGB channels, the values from all three channels of each pixel are arranged sequentially. This process is applied across the entire image, resulting in a flattened 1-D representation. For a total of n images, all having the same resolution, these 1-D vectors are collected into a matrix X, where each row corresponds to a vectorized image of length d, as referenced in the following equation:

$$X = \begin{bmatrix} x_{11} & x_{12} & \cdots & x_{1d} \\ x_{21} & x_{22} & \cdots & x_{2d} \\ \vdots & \vdots & \ddots & \vdots \\ x_{n1} & x_{n2} & \cdots & x_{nd} \end{bmatrix} \tag{2.7}$$

Next, a centered data matrix $\tilde{X}$ ($n \times d$ matrix is obtained by subtracting means from each image vectors, as shown in Equation 2.8, where μ is a $1 \times d$ vector that contains means from each column of matrix X ($1\mu^T$ leads to a $n \times d$ matrix that broadcasts μ to every row of X) [3].

$$\tilde{X} = X - 1\mu^T, \quad \mu = \frac{1}{n}\sum_{i=1}^{n} x_i \tag{2.8}$$

The covariance matrix C of the centered data matrix $\tilde{X}$($n \times d$ matrix can be derived shown in Equation 2.9. Before computing the principal components, eigenvalues and eigenvectors of the covariance matrix C are derived using Equation 2.10 where v_k is the k^{th} eigenvector of d dimensions, and λ_k is the corresponding eigenvalue. After that, eigenvalues are arranged in descending order, presented in Equation 2.11.

$$C = \frac{\tilde{X}^T \tilde{X}}{n} \tag{2.9}$$

$$Cv_k = \lambda_k v_k, \quad k = 1, 2, ..., d \tag{2.10}$$

$$\lambda_1 \geq \lambda_2 \geq \cdots \geq \lambda_d \tag{2.11}$$

For a simple visualization, only the first two principal component (PC) values, PC1 and PC2, are calculated for each image. Therefore, v_1 and v_2, which are associated with λ_1 and

λ_2, represent the directions of maximum variance, are selected to form a $d \times 2$ matrix W in Equation 2.12. To obtain the PC1 and PC2 values for each image, the centered data matrix $\tilde{X}$ is projected onto the matrix W in Equation 2.13. X_{proj} is an $n \times 2$ matrix that contains PC1s ($(X_{proj})_{i1}$) and PC2s ($(X_{proj})_{i2}$) for all the images. To find out how much variance of the data explained by PC1 and PC2, the largest and second largest eigenvalues (λ_1 and λ_2) are simply divided by the sum of all the eigenvalues obtained from the covariance matrix C, as shown in Equation 2.14.

$$W = [v_1, v_2] \tag{2.12}$$

$$X_{proj} = \tilde{X}W \tag{2.13}$$

$$\frac{\lambda_1}{\sum_{k=1}^{d} \lambda_k}, \quad \frac{\lambda_2}{\sum_{k=1}^{d} \lambda_k} \tag{2.14}$$

2.2 Materials and Datasets

2.2.1 Metallic Microstructures

To help characterize microstructural shape and topology, two distinct metallic microstructures have been analyzed: Titanium-Aluminum alloys (Ti-Al) and Nickel Chromium-based superalloy known as Inconel 718. The Titanium-Aluminum (Ti-Al) alloy system exhibits exceptional mechanical strength and low density, as well as outstanding high-temperature stability and exceptional corrosion resistance [9]. Such properties make them particularly advantageous for aerospace and automotive applications, as well as in the biomedical field, where lightweight and high tensile strength are critical in mechanical engineering. Inconel superalloys, as defined by extreme oxidation, corrosion, and thermal resistance, have become

indispensable in critical power generation, aerospace, nuclear, and even chemical process industries due to their resilience in the harshest environments [4].

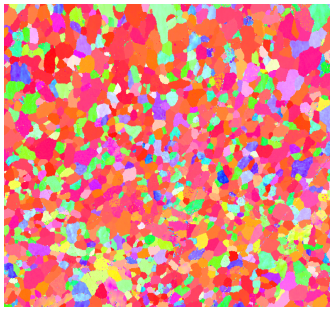

(a) Ti-0Al under 600°C for 1hr

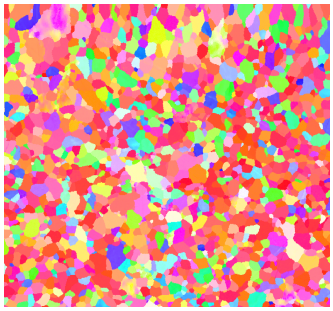

(b) Ti-0Al under 600°C for 1.5hr

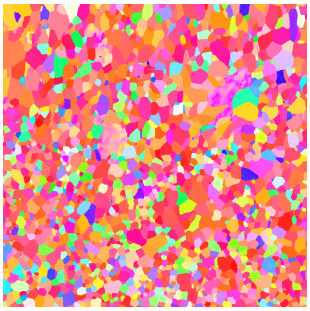

(c) Ti-0Al under 800°C for 30sec

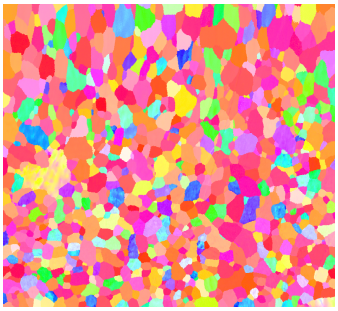

(d) Ti-0Al under 800°C for 45sec

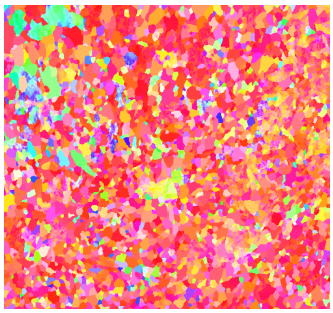

(e) Ti-4Al under 800°C for 40min

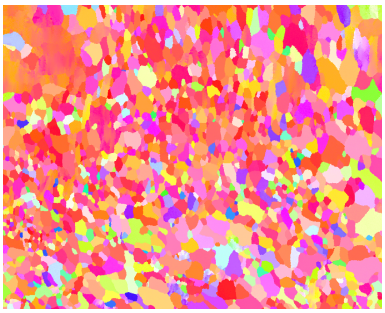

(f) Ti4Al under 800°C for 2hr

(g) Ti-7Al under 800°C for 72hr

(h) Ti-7Al under 800°C for 96hr

Figure 2.1: Experimental (EBSD) images of Titanium-Aluminum Alloy microstructures

The Ti-Al dataset applied in this research examines static recrystallization kinetics in three distinct alpha-Titanium alloys with varying in Aluminum content: Ti-0Al, Ti-4Al, and Ti-7Al (Al in weight %). These samples were deformed via compression at ambient temperature and subsequently annealed in an air environment within a tube furnace at temperatures between 500°C and 800°C, and the annealing time varied from 10 seconds up to 96 hours across all alloys [5]. Crystallographic orientations, grain morphology, and recrystallization progress were visualized through Inverse Pole Figure (IPF) maps obtained from electron backscatter diffraction (EBSD) data. To assess the robustness and effectiveness of the microstructural shape and topology characterization methods mentioned previously, eight IPF images with a reduced amount of noise were selected, two representing each alloy variant, as shown in Fig. 2.1. These IPF images were then cropped into smaller pieces for computational efficiency and data augmentation.

In addition to experimentally obtained EBSD images, this study also incorporates synthetic microstructural images generated by deep learning models, the Progressive Generative Adversarial Network (PGAN) and the Denoising Diffusion Probabilistic Model (DDPM), to evaluate the capability of previously described characterization approaches. Fig. 2.2 shows a random Ti-Al microstructure from experimental Ti-Al dataset, as well as from each deep learning generated groups. PGAN employs a gradual training protocol, initially focusing on lower-resolution outputs and incrementally scaling complexity, which promotes stable learning of complex microstructural features, resulting in synthetic images that closely match real microstructures visually [11]. On the other hand, DDPM synthesizes images by progressively adding and systematically removing noise, enabling the generation of highly detailed images with superior representation of global grain structures and topology, although sometimes exhibiting less local texture and color accuracy relative to PGAN outputs [11]. Initially, experimental microstructure images of all three alpha-Titanium alloys are randomly selected.

The same images are then fed to both deep learning models, and 200 synthetic images are generated from each of them. Utilizing synthetic images enriches experimental datasets, enables more comprehensive exploration of microstructural variability, and improves predictions of material performance. Evaluating the ability of microstructural characterization methods to differentiate synthetic data from real images is essential for verifying the effectiveness of computational models and the reliability of synthetic data for applications in materials engineering.

(a) Randomly selected experimental Ti-Al microstructure (EBSD data)

(b) Randomly selected Ti-Al microstructure generated by the PGAN model

(c) Randomly selected Ti-Al microstructure generated by the DDPM model

Figure 2.2: Synthetic images generated for Titanium-Aluminum alloy samples

The Inconel alloy dataset used in the study is a wrought Inconel 718 Nickel-based superalloy, which is mostly composed of Nickel, Chromium, Iron, and Niobium, with minor contributions from Aluminum, Cobalt, Titanium, Carbon, and Nitrogen [17]. The alloy was initially annealed at 1050°C for half an hour, then rapidly cooled via water quenching, resulting in a uniform grain structure with an average grain size of approximately 62 μm [17]. A subsequent dual-stage precipitation-hardening treatment was applied to optimize mechanical performance. Mechanical deformation tests were conducted at room temperature on dogbone-shaped tensile specimens until achieving around 1.26% plastic strain [17]. After that, 2-D IPF orientation maps derived from EBSD were used to characterize grain orientations. To systematically investigate how image resolution influences the results obtained

from Hu moment, PEM, and PCA analyses, raw IPF images captured along the X-direction are segmented into multiple window sizes, as presented in Fig. 2.3.

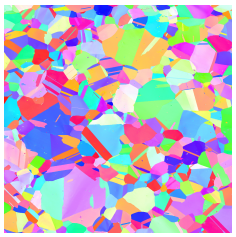

(a) Original Inconel-718 microstructure

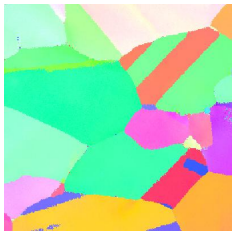

(b) Example synthetic image created with a window size of 400×400

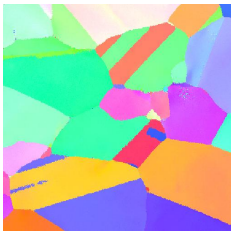

(c) Example synthetic image created with a window size of 500×500

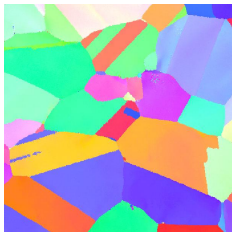

(d) Example synthetic image created with a window size of 600×600

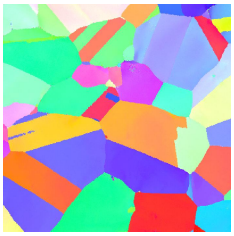

(e) Example synthetic image created with a window size of 700×700

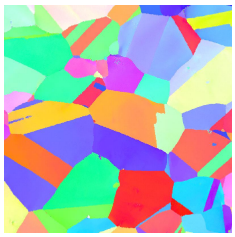

(f) Example synthetic image created with a window size of 800×800

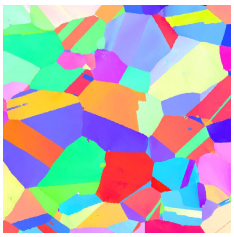

(g) Example synthetic image created with a window size of 900×900

Figure 2.3: Inconel-718 microstructures generated with different window sizes

2.2.2 Mechanical Metamaterials with Unit Cell and Spinodoid Topologies

Two approaches to engineering the microstructural topologies of mechanical metamaterials involve unit cell and nature-inspired spinodal designs. Unit cells are the basic building blocks of periodic structures, typically designed with precise geometric control to form representative volume elements (RVEs) that can be repeated across a domain [24, 25]. This type of periodicity is advantageous as it aids in the design process and enables efficient simulation through homogenization techniques [24, 25]. Widely used in lightweight structural applications, unit cell-based metamaterials are beneficial due to their high strength-to-weight ratio and ease of design, which results in excellent resistive structural adaptability and are excellent for optimization [24, 25]. Spinodal structures incorporate continuous and smooth topologies, non-periodic in nature, leaning towards the natural process of spinodal decomposition [26, 36]. The structure is created using Gaussian Random Fields (GRF) to imitate the early-phase stage of geometrical separation, resulting in solid and void regions [26, 36]. In contrast to conventional truss or lattice-based metamaterials, spinodoids possess improved resistance to mechanical stress and deformation due to the minimization of stress concentrations[26, 36]. Continuity in the topology of such structures enables unique mechanical responses, such as highly tunable anisotropic behavior, negative Poisson's ratio, and attractive application potential in the aerospace industry, biomedical implants, and other military and civilian applications [26, 36].

As presented in Fig. 2.4, 5 unit cells and 64 spinodoids images are used in this study to assess the application, efficacy, and generalizability of the proposed shape and topology characterization techniques. Their periodic and non-periodic architectures provide a range of structural diversity, which helps determine the effectiveness of the methods for quan-

tifying topological differences. The use of these materials not only serves to validate the proposed methods but also enhances the insight into the connections between topology and performance in advanced engineering materials.

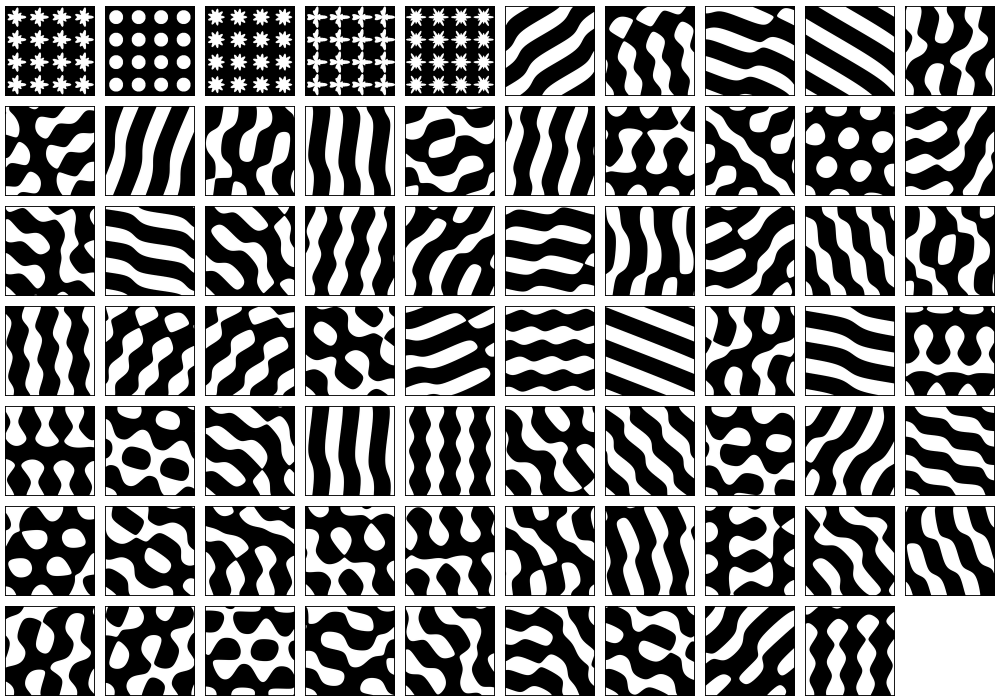

Figure 2.4: Example topologies for unit cell and spinodal (spinodoids) metamaterials

Chapter 3

Results and Discussion

This chapter presents the results of a data-driven approach to classifying shapes and topologies of distinct microstructures using Hu moments, Principal Eigenvalue Moments (PEM), and Principal Component Analysis (PCA). The representative examples of materials data are focused on Titanium-Aluminum alloy microstructures, synthetic images of microstructures generated by machine learning models (Denoising Diffusion Probabilistic Models (DDPM) and Probabilistic Generative Adversarial Networks (PGAN)), Inconel-718 alloy microstructures, and computationally created metamaterials designs with unit-cell and spinodoid topologies. The analysis demonstrates the capability of differentiating microstructures based on their shapes, characterizing the realism of synthetic microstructures relative to experimental microstructure data, and examining the influence of analytical parameters, such as window size, on the characterization process.

3.1 Results with Hu Moments and Principal Eigenvalue Moment

3.1.1 Results for Metallic Microstructures

First, the numerical results are generated using Hu moments. Since the first two Hu moments capture the most shape information due to the declining order of captured information with increased order, they are used to characterize and cluster microstructures. In particular,

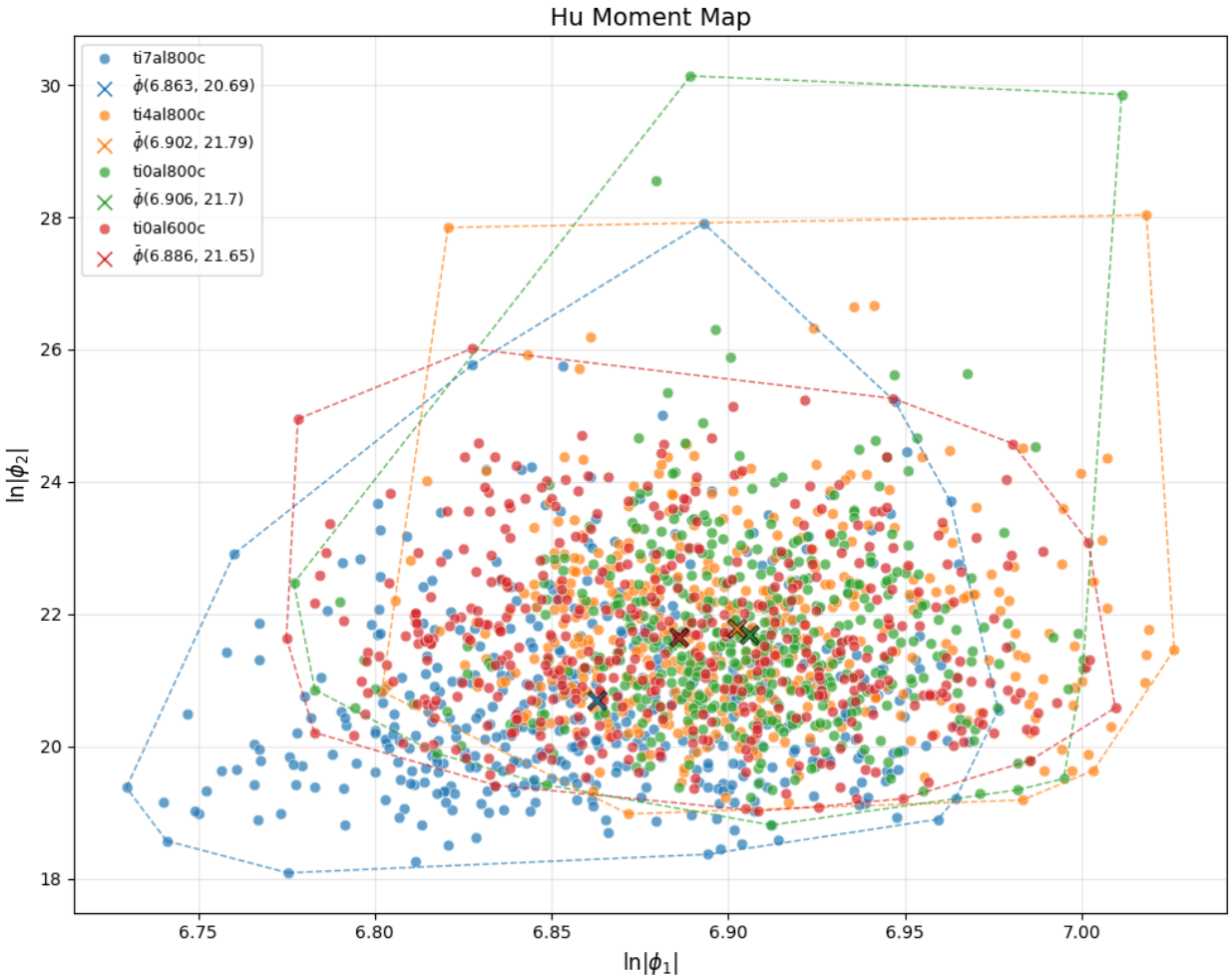

Figure 3.1: Hu moment map for the experimental data of Titanium-Aluminum alloys

Table 3.1: Hu moment statistical analysis for the experimental data of Titanium-Aluminum alloys

	Max Variation		STD Deviation	
Group	1st Hu	2nd Hu	1st Hu	2nd Hu
Ti7Al at 800 °C	0.1332	7.2127	0.0510	1.3725
Ti4Al at 800 °C	0.1240	6.2430	0.0442	1.3330
Ti0Al at 800 °C	0.1290	8.4402	0.0364	1.3741
Ti0Al at 600 °C	0.1234	4.3562	0.0509	1.2995

the first two Hu moments are second order and represent ellipticity and shape asymmetry. Fig. 3.1 shows the Hu moment map of the Titanium-Aluminum alloy microstructures. The first Hu moment is on the X-axis and the second one is on the Y-axis. Four groups are selected for this plot: Ti-0Al data obtained at 600°C, Ti-0Al data obtained at 800°C, Ti-4Al data obtained at 800°C, and Ti-7Al data obtained at 800°C. As the plot shows, the first Hu moment ranges from 6.7 to 7.05, and the second Hu moment varies from 18 to 30. Convex hulls are applied to better distinguish the area for each cluster, and the mean value is highlighted for comparing similarities in average/expected shape statistics. The max variations and standard deviations for each Ti-Al group of this dataset are also calculated and shown in Table 3.1. Max variation measures the largest distance from mean values, and standard deviation measures how dispersed the data is in relation to the mean [1].

It can be seen that the Ti-4Al under 800°C treatment temperature and Ti0Al under 800°C appear to have very similar mean values for both the first and second Hu moments, with the first Hu moment values of 6.902 and 6.906, and the second Hu moment values of 21.79 and 21.7. The first Hu moment reflects the overall distribution of pixel intensities. Here, a larger first Hu moment value indicates more spread-out or dispersed shapes. The second Hu moment reflects elongation and skewness of a shape, where a lower second Hu moment often represents more circular and symmetrical shapes. Therefore, we can conclude that the grain

sizes and shapes for these two groups of Titanium-Aluminum alloys are similar to each other. Compared with Ti-4Al at 800°C, although Ti-0Al at 600 °C has a second mean Hu moment value closer to Ti-0Al at 800°C (with differences of 0.05 vs 0.09), it has a larger difference in terms of the first Hu moment value (with differences of 0.02 vs 0.004, respectively). This phenomenon indicates that while Ti-0Al alloys are similar in grain shapes, the Ti-4Al alloy samples have a closer average grain size under the same temperature and time treatments.

Among the groups, the Ti-7Al alloy has the smallest mean value for both Hu moments. This indicates a condensed pixel intensity and lower eccentricity, or larger grain sizes and more circular and symmetrical grain shapes. It can be clearly seen from the EBSD images in Fig. 2.1, as each individual grain for Ti-0Al and Ti4-Al appears much smaller compared to the grains of Ti-7Al. This situation can also be a result of the different post-treatment times. In Fig. 2.1, images on the right side contain larger grains than the left, which shows that Titanium-Aluminum alloys tend to have larger grain sizes with longer treatment times under the same temperature. The treatment time for Ti-7Al alloy is much longer than other groups, which makes its grain size larger and thus supports what's shown in the Hu moment plot.

Table 3.2: PEM statistical analysis for the experimental data of Titanium-Aluminum alloys

	Max Variation		STD Deviation	
Group	1st PEM	2nd PEM	1st PEM	2nd PEM
Ti7Al at 800 °C	0.1613	0.1451	0.0549	0.0547
Ti4Al at 800 °C	0.1372	0.1403	0.0447	0.0474
Ti0Al at 800 °C	0.1279	0.1410	0.0373	0.0402
Ti0Al at 600 °C	0.1284	0.1377	0.0502	0.0554

Moving forward to the principal eigenvalue moment, since it is a result of eigenvalues from the first and second Hu moments, the PEM value will capture the spread of the pixel intensities along the principal axes of the grains. Therefore, a closer PEM mean value represents closer

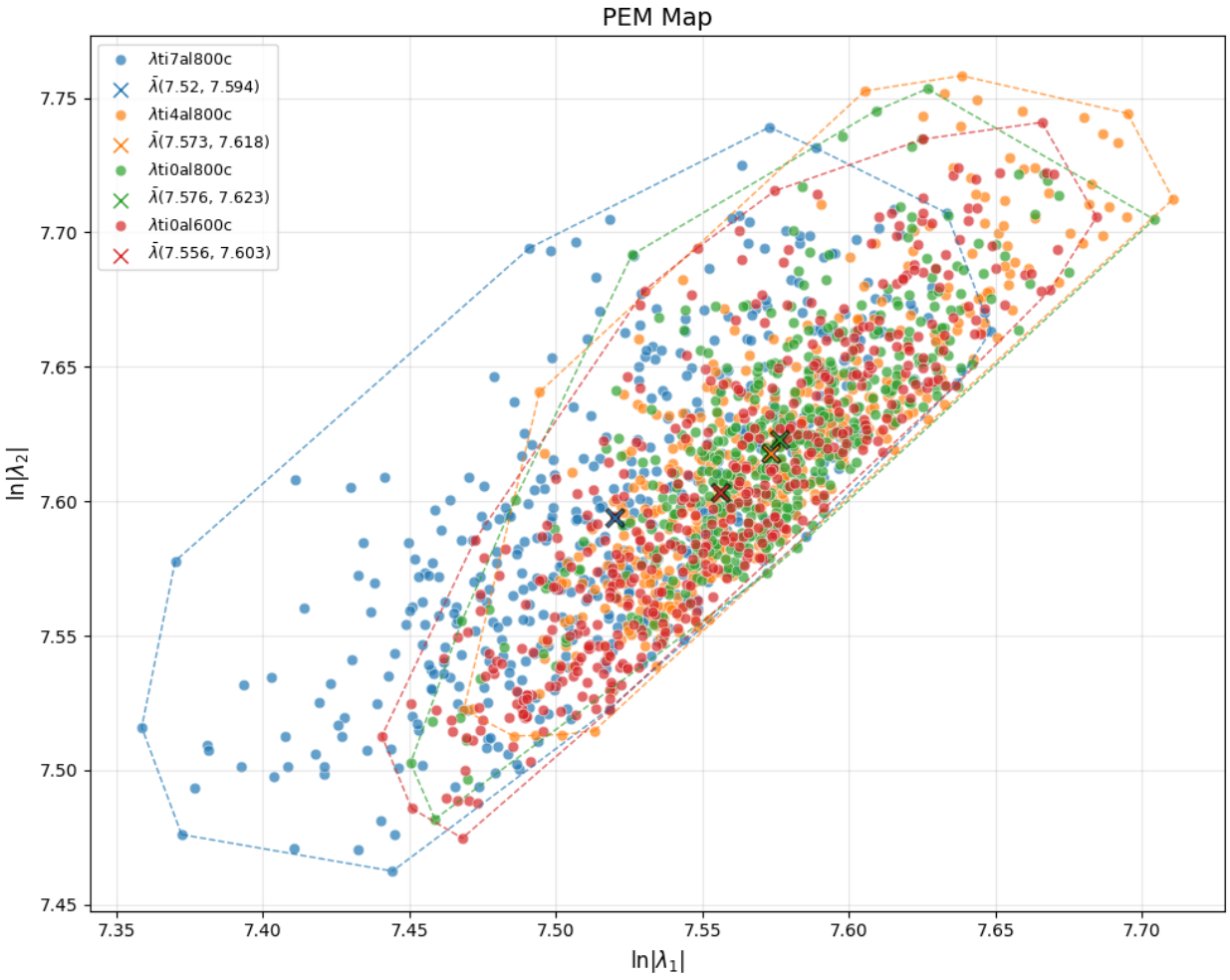

Figure 3.2: Principal Eigenvalue Moment (PEM) map for the experimental data of Titanium-Aluminum alloys

microstructure characteristics. In Fig. 3.2, the mean data points of Titanium-Aluminum alloy groups agree with what's shown on the Hu moment plot, as the "Ti7Al800C(Blue)" clearly differentiated from other groups, and "Ti4Al800C(Orange)" and "Ti0Al800C(Green)" have the closest mean values. In addition, since PEM combines the first and second Hu moments into a single scalar, the resulting value would have a smaller variation or spread across the map, which can be observed from the Table 3.2 that the max variations and std deviations of the 2nd PEMs for all Ti-Al groups are much smaller compared to the corresponding values of the 2nd Hu moments in Table 3.1.

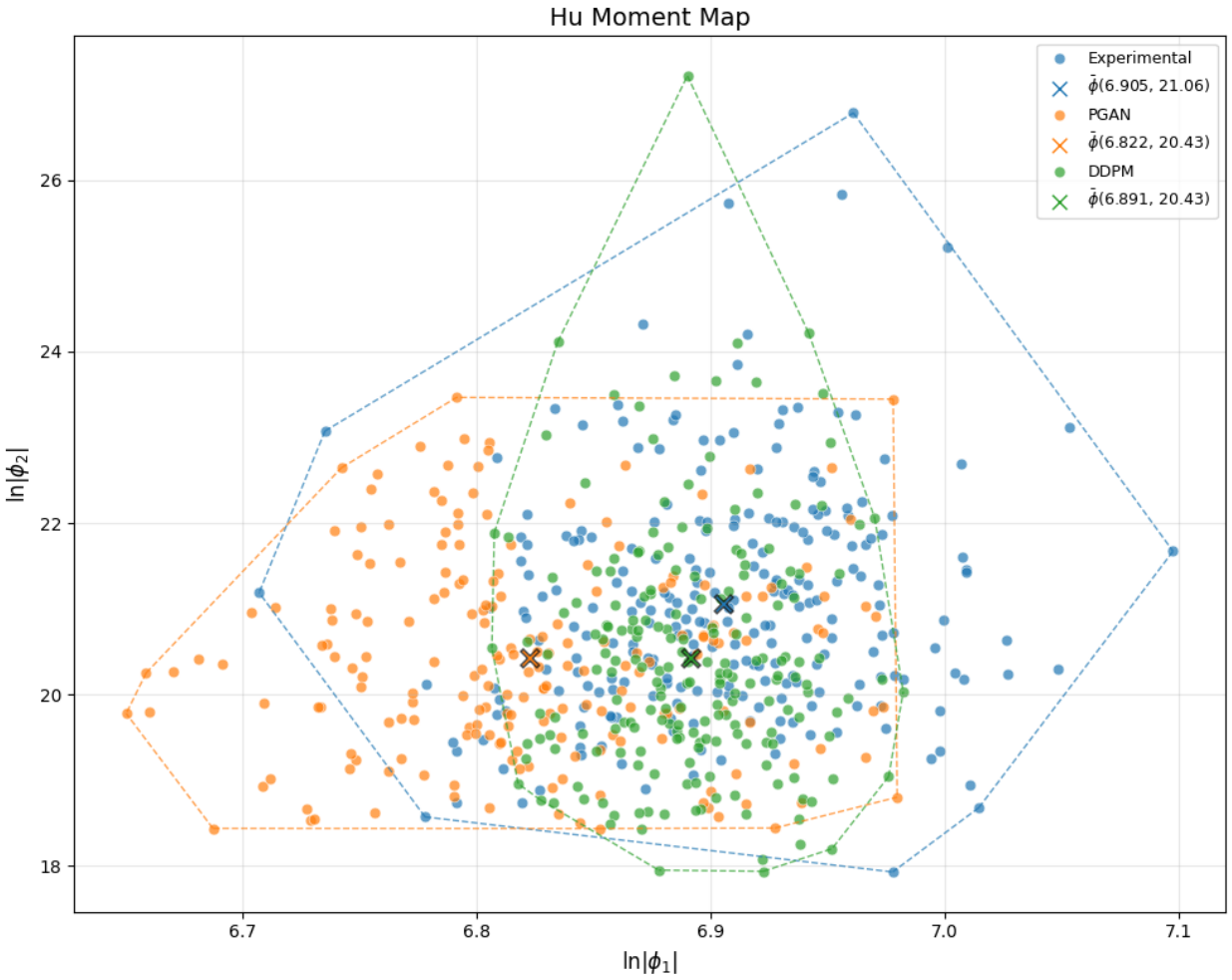

Figure 3.3: Hu Moment maps of experimental and synthetic data of Titanium-Aluminum alloys

While Hu moments work well in quantifying experimental microstructure images, they can also be used to compare synthetic images. Fig. 3.3 shows the result of the synthetic Ti-Al data generated by machine learning models, denoising diffusion probabilistic model (DDPM), and probabilistic generative adversarial network (PGAN), as well as the real experimental image data. By comparing the mean value data points, the DDPM group has a closer first Hu moment to the experimental group than the PGAN. This could indicate that the grain distribution generated by DDPM appears more realistic than that from PGAN. However, both DDPM and PGAN have the same values for the second Hu moment, indicating that

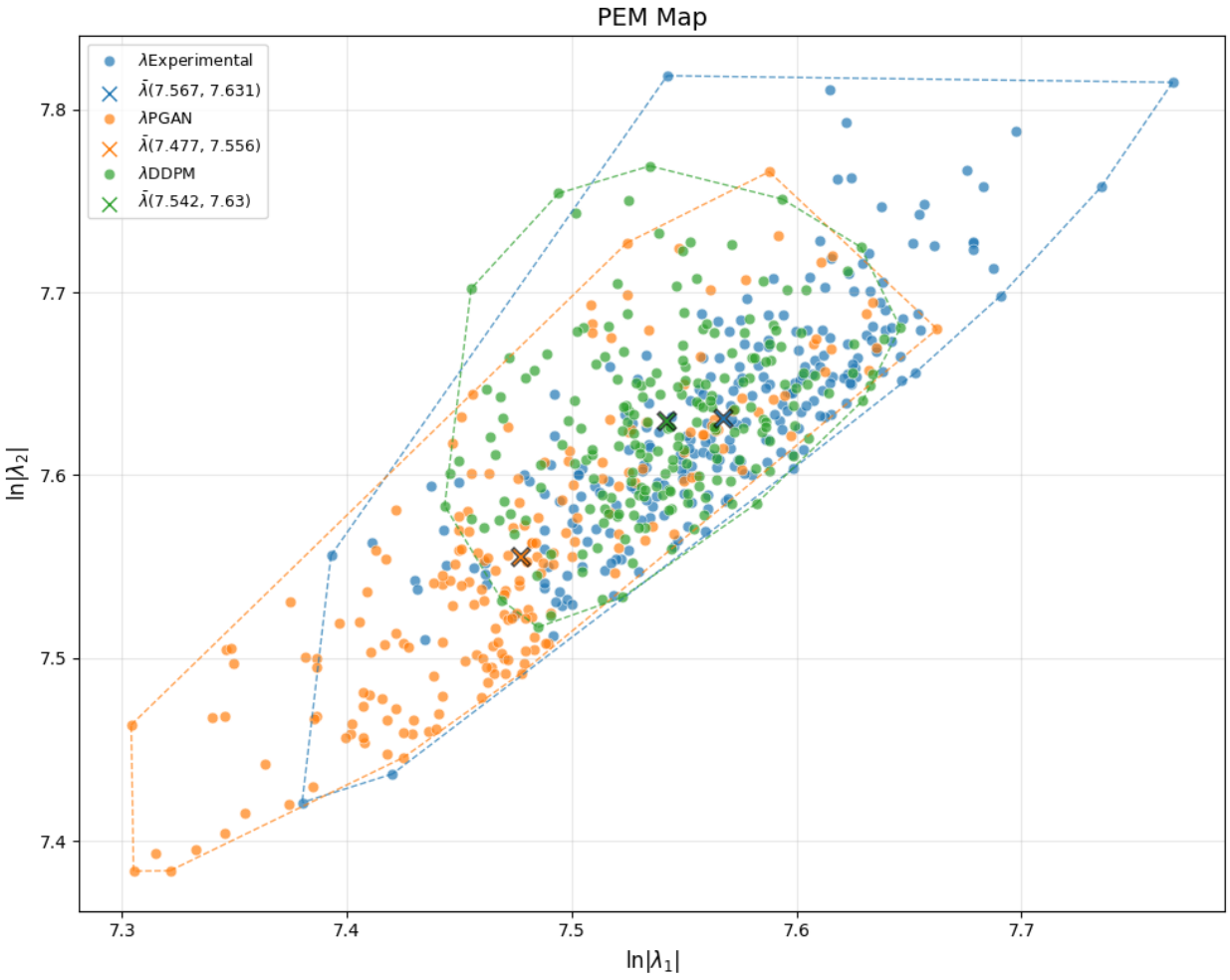

Figure 3.4: Principal Eigenvalue Moment (PEM) maps of experimental and synthetic data of Titanium-Aluminum alloys

the shape they are generating is similar to each other, while a gap still exists between the synthetic and experimental microstructure. This phenomenon can be seen from Fig. 2.2. Aside from the color differences, which the Hu moment calculation does not take into account, the DDPM-generated microstructure seems to have clearer grain boundaries than the ones from PGAN. However, the grain shapes for both PGAN and DDPM are similar to each other and close to the experimental microstructure via a simple visual check.

The corresponding PEM map reflects the same situation with the Hu moment maps, where

Table 3.3: Hu statistical analysis for the synthetic data of Titanium-Aluminum alloys

	Max Variation		STD Deviation	
Group	1st Hu	2nd Hu	1st Hu	2nd Hu
Experimental	0.1923	5.6966	0.0588	1.3095
PGAN	0.1720	3.0325	0.0702	1.1585
DDPM	0.0909	6.7914	0.0368	1.3897

Table 3.4: PEM statistical analysis for the synthetic data of Titanium-Aluminum alloys

	Max Variation		STD Deviation	
Group	1st Hu	2nd Hu	1st Hu	2nd Hu
Experimental	0.1997	0.1938	0.0618	0.0610
PGAN	0.1853	0.2101	0.0703	0.0767
DDPM	0.1043	0.1393	0.0424	0.0472

the mean value for DDPM is closer to the experimental mean value, indicating a closer microstructure characteristic. Moreover, the DDPM cluster on the PEM map appears to have a more condensed spread compared to the PGAN cluster, which indicates that DDPM-generated microstructures are more consistent. This can also be seen in Table 3.4 where the max variation and standard deviation for DDPM are much smaller compared to the corresponding values for PGAN.

The effect of different window sizes is also investigated using samples of Inconel-718 alloy. The original 3000 by 2985 pixel microstructure image is cropped into pieces with different window sizes each time from 400 by 400 to 900 by 900, as shown in Fig. 2.3. The results presented in Fig. 3.5 and Fig. 3.6 share the same pattern. As the resolution increases, the spread of the data points tends to be narrower (although some variations appear on the Hu moment map), and the convex hull area also decreases. This is because increasing the window size causes more overlapping pixel values and thus reduces the overall complexity of the data. This can be observed clearly in Table 3.6, where the max variations and standard

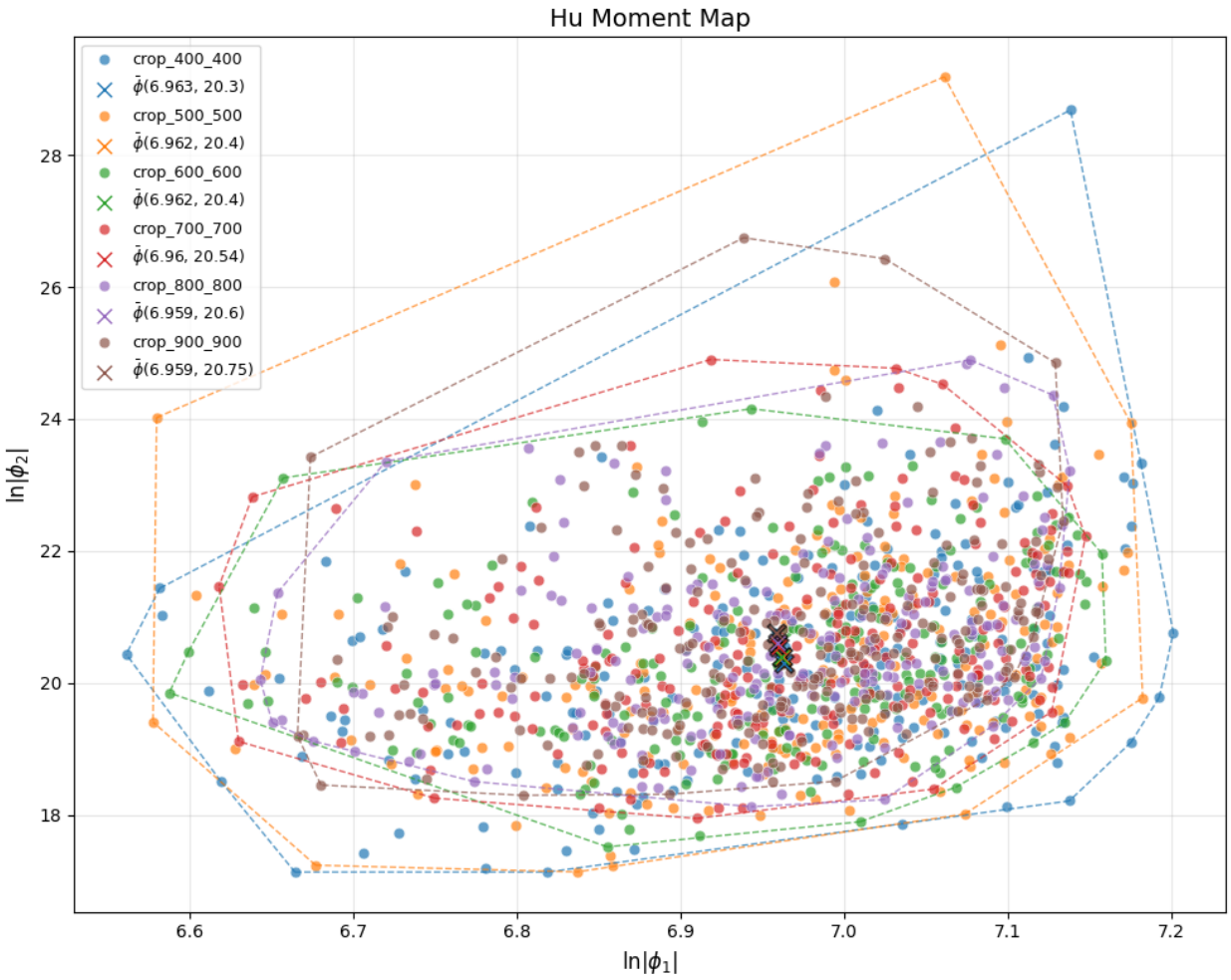

Figure 3.5: Hu moment maps for microstructures created with different window sizes

Table 3.5: Hu statistical analysis with different window sizes

	Max Variation		STD Deviation	
Group	1st Hu	2nd Hu	1st Hu	2nd Hu
400x400	0.4020	8.3803	0.1371	1.5360
500x500	0.3846	8.7835	0.1291	1.6424
600x600	0.3740	3.7545	0.1226	1.2925
700x700	0.3422	4.3583	0.1172	1.3841
800x800	0.3162	4.3000	0.1127	1.3030
900x900	0.2927	5.9914	0.1083	1.4328

deviations are decreasing as the window size increases. Even though the window size varies, the overall means for each group are very close to each other on both Hu moment and PEM maps since the analysis is conducted using the same microstructure image, and Hu moment and PEM are scale invariants. In addition, a good way to determine the appropriate cropping size is to observe the contours on the PEM map. For example, for this dataset, the contour of the cluster shifts much less and tends to converge when the cropping size reaches 700 by 700, which means a good window size would be at least 700 by 700 to better capture the information.

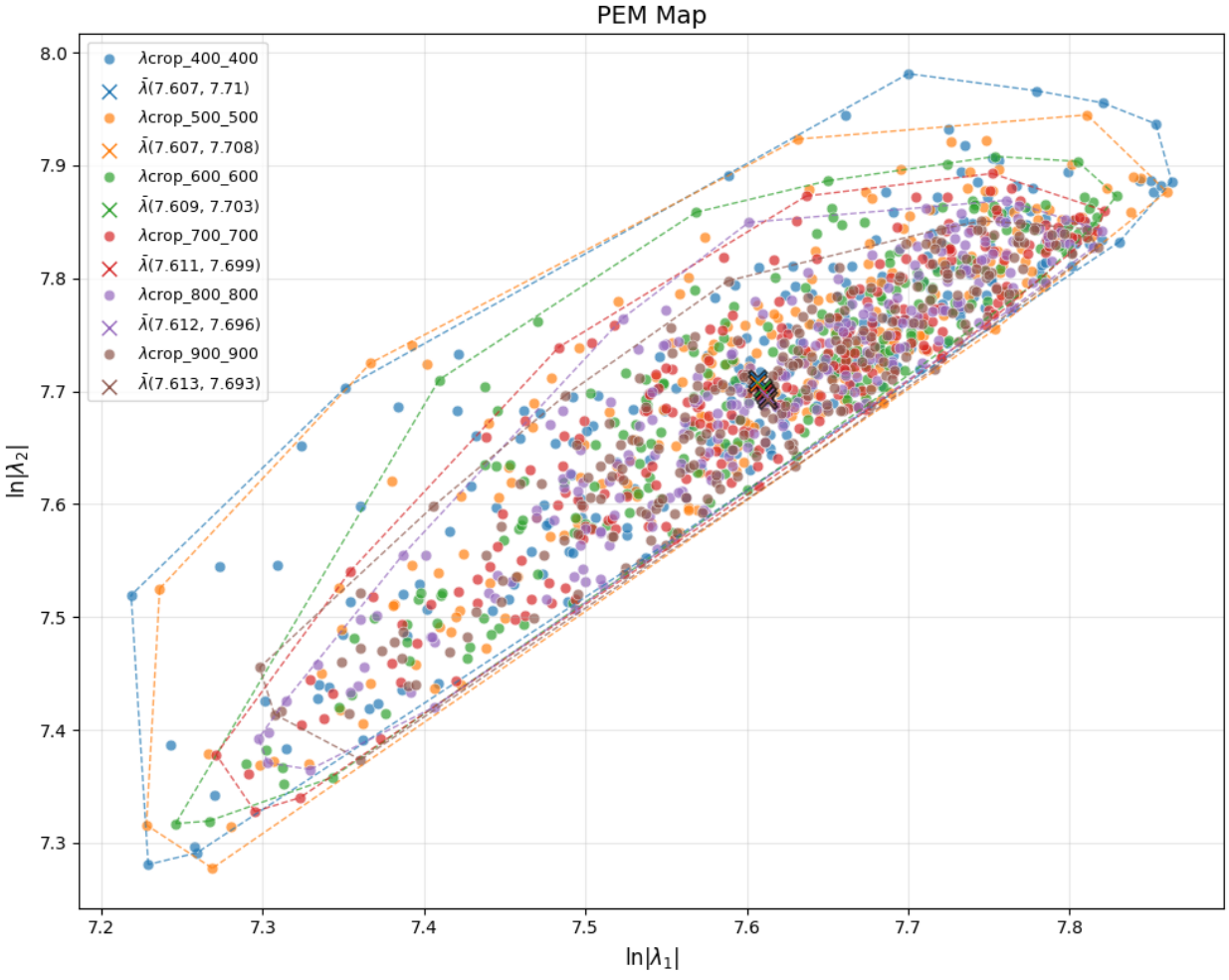

Figure 3.6: PEM maps for microstructures created with different window sizes

Table 3.6: PEM statistical analysis with different window sizes

	Max Variation		STD Deviation	
Group	1st PEM	2nd PEM	1st PEM	2nd PEM
400x400	0.3883	0.4295	0.1458	0.1354
500x500	0.3793	0.4304	0.1362	0.1297
600x600	0.3634	0.3862	0.1267	0.1244
700x700	0.3396	0.3714	0.1215	0.1183
800x800	0.3143	0.3308	0.1169	0.1128
900x900	0.3151	0.3190	0.1133	0.1071

3.1.2 Results for Unit Cells and Spinodoids

Figure 3.7 shows the Hu moment results for the unit cells and spinodoids. The raw images are directly placed on top of the data points for a better visualization of the classification. In the plot, the data points exhibit noticeable dispersion across both the first and second Hu moment axes. For the 5 unit cell images, they all share a very close first Hu moment value, as they line up vertically at the left side of the plot. This is because the first Hu moment reflects the distribution of pixel intensity, and all of the 5 unit cell images contain a similar amount of solids (in this case, black pixels) around the corresponding locations across the image. The unit cell with circular voids (white pixels) in the top left corner is separated away from the other unit cells with non-circular voids, and further consolidates the fact that the second Hu moment tests the ellipticity of the shapes, thus a shape close to a circle receives a higher second Hu moment value. Similar patterns are exhibited on the spinodoid data as well, as spinodoids with similar topologies are close to each other: spinodoids with circular voids are at the bottom left and bottom right, spinodoids with line-shaped voids are at the right side, and the rest of the spinodoids with wave-shaped voids cluster in between.

Looking at the PEM map for the unit cells and spinodoids displayed in Fig. 3.8, the Hu moment results are flipped diagonally and compressed vertically along the y-axis. Referring

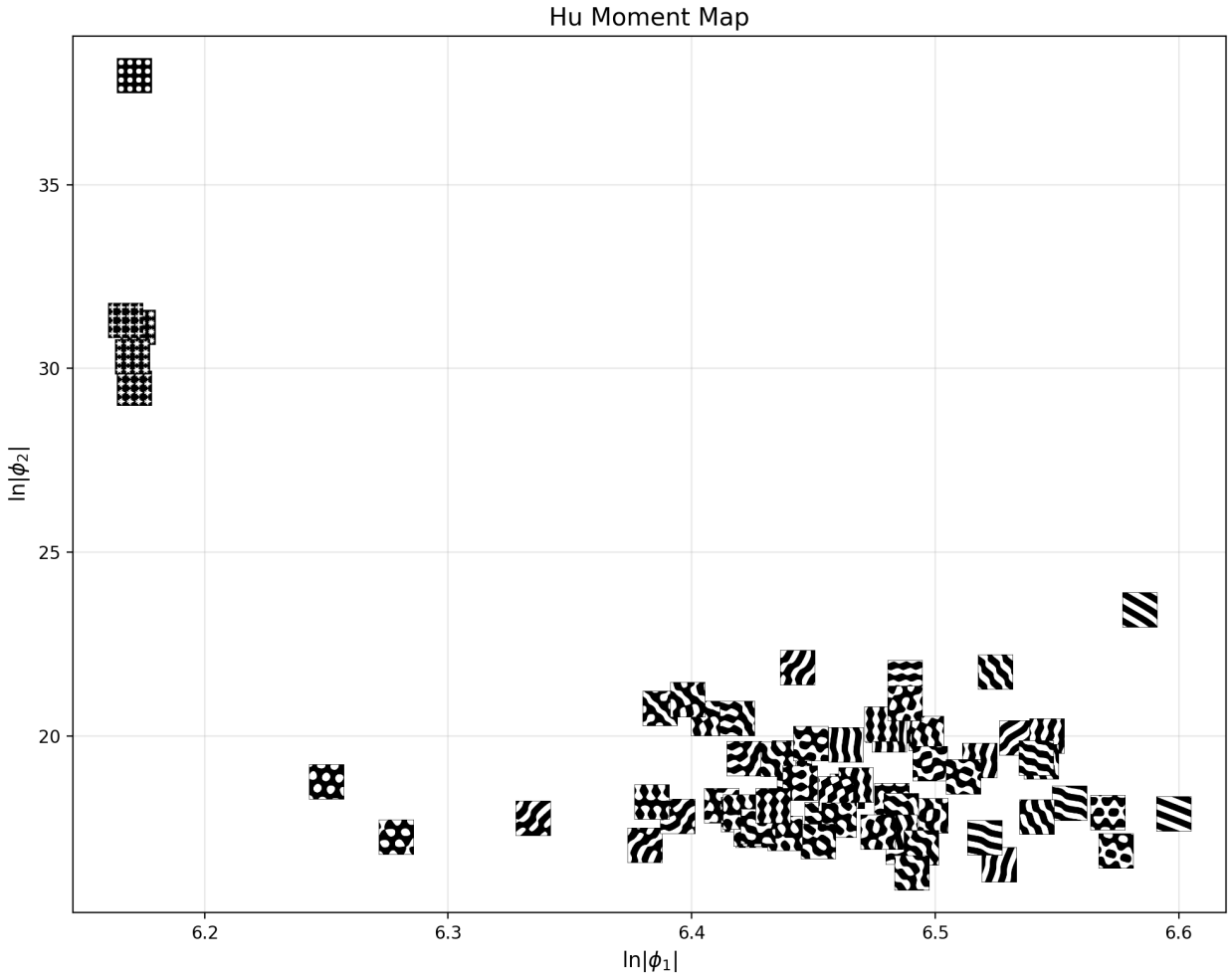

Figure 3.7: Hu moment map for spinodoid materials

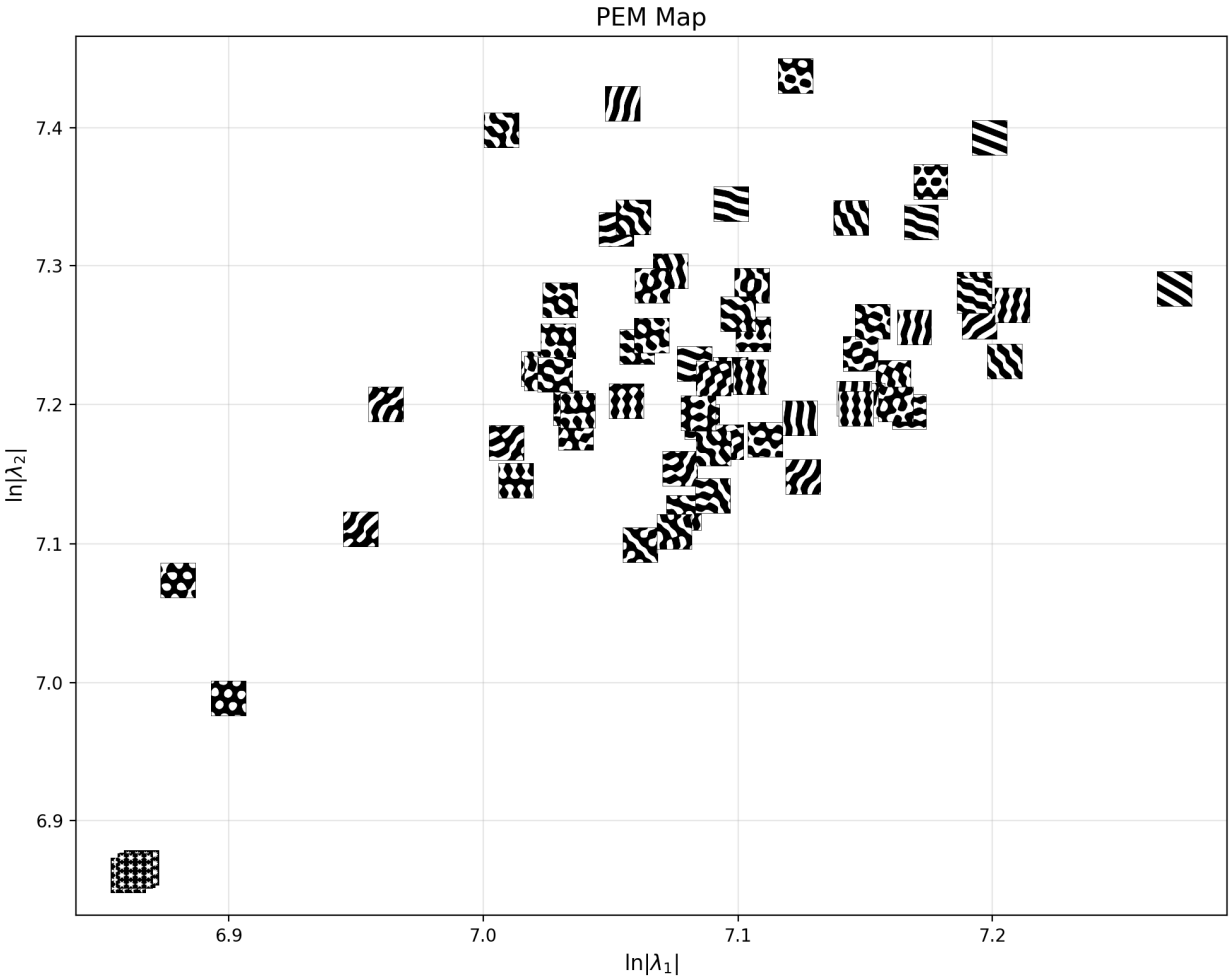

Figure 3.8: PEM map for spinodoid materials

back to the section 2.2.1, where the PEM is defined as a combination of the first and second Hu moments, it is reasonable to see this result in the figure. Despite the changes in the images, PEM is able to separate unit cells from spinodoids and classify spinodoids with closer topology.

3.2 Principal Component Analysis (PCA)

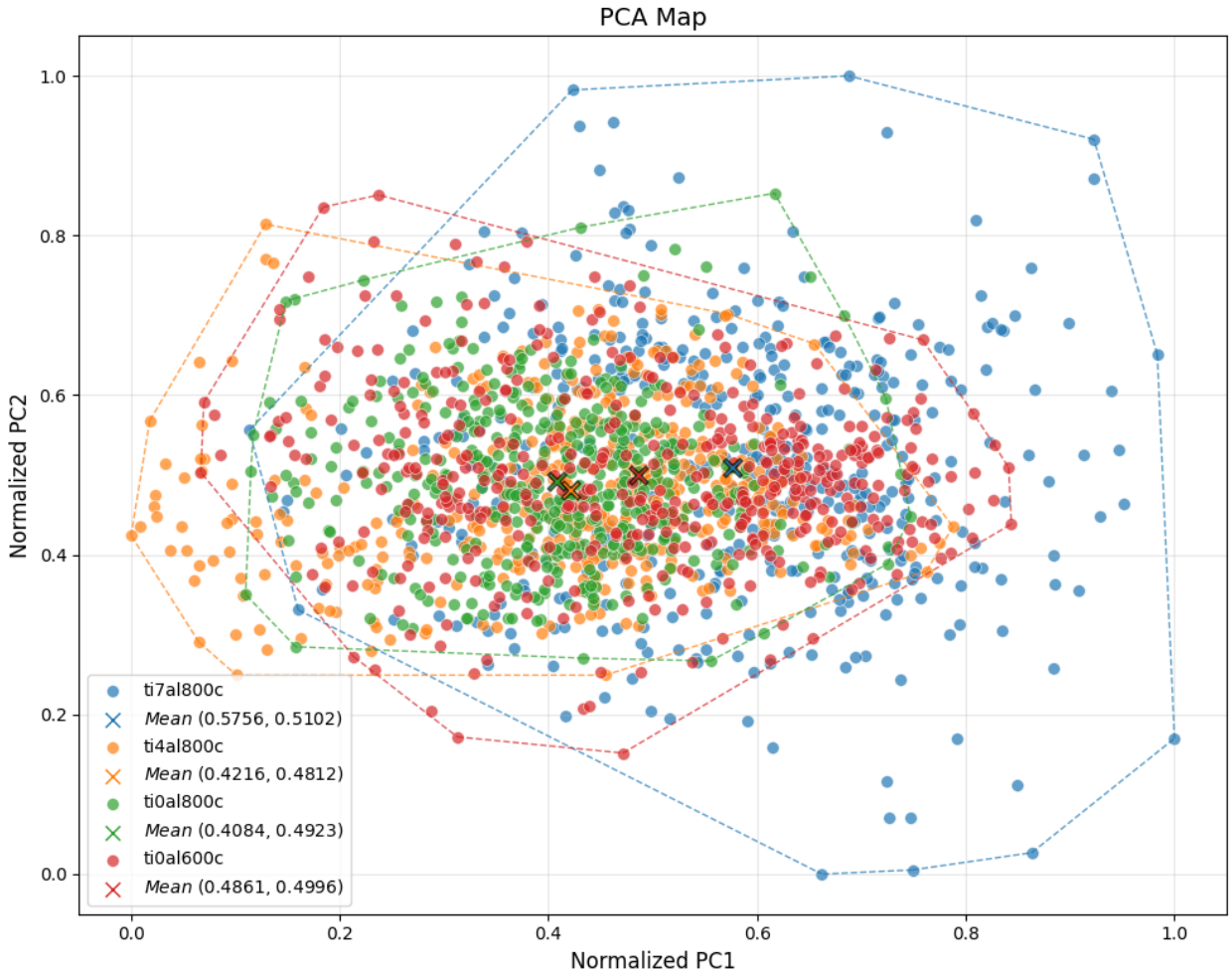

Figure 3.9: PCA Map for experimental Titanium Aluminum microstructures (grayscale)

Table 3.7: PCA (Grayscale) statistical analysis for the experimental data of Titanium-Aluminum alloys

	Max Variation		STD Deviation	
Group	PC1	PC2	PC1	PC2
Ti7Al at 800 °C	0.4622	0.5122	0.1636	0.1604
Ti4Al at 800 °C	0.4215	0.3338	0.1586	0.0953
Ti0Al at 800 °C	0.3385	0.3621	0.1148	0.0959
Ti0Al at 600 °C	0.4189	0.3508	0.1760	0.1056

3.2.1 Results for Metallic Microstructures

While the Hu moment invariant is considered a promising approach for quantifying microstructure images, its results are compared to the principal component analysis (PCA), which is a widely used dimension reduction technique. In a regular PCA map as shown in Fig. 3.9, the first two principal components are calculated and normalized for each image and plotted on the X and Y axes, and the convex hull is applied to each group of data. The corresponding max variations and standard deviations for each group are calculated and shown in Table 3.7.

In Fig. 3.9, the same experimental Titanium-Aluminum microstructure images are used as in Fig. 3.1 and Fig. 3.2. Although the outline of the data looks different, the mean principal component (PC) values appear to have similar patterns with the corresponding Hu moment plots. The average for "ti0al800C" (green) is closer to "ti4al800C" (orange) than "ti0al600C" (red), and the one for "ti7al800C" (blue) can be clearly separated from the others. The bigger difference in PC1 values is due to the fact that the first principal component captures most of the variance, in this case, 4.28 percent of the data. Moreover, PC2 is found to capture 2.40 percent of the variance.

However, since PC1 and PC2 only add up to around 6.68 percent of variance, it means that

the original data contains significant variability. And by calculation, the total number of principal components required to describe 95 percent of the variance is found to be 510. This result seems common in high-dimensional image data, especially for polycrystalline microstructures, because the pixel intensity can vary dramatically across grains. Also, the total number of principal components is determined by the dimension of the image, which in this case is 2,500 for each image. Although most of the variance is not represented by the PCA map, it is useful for visualizing broad patterns.

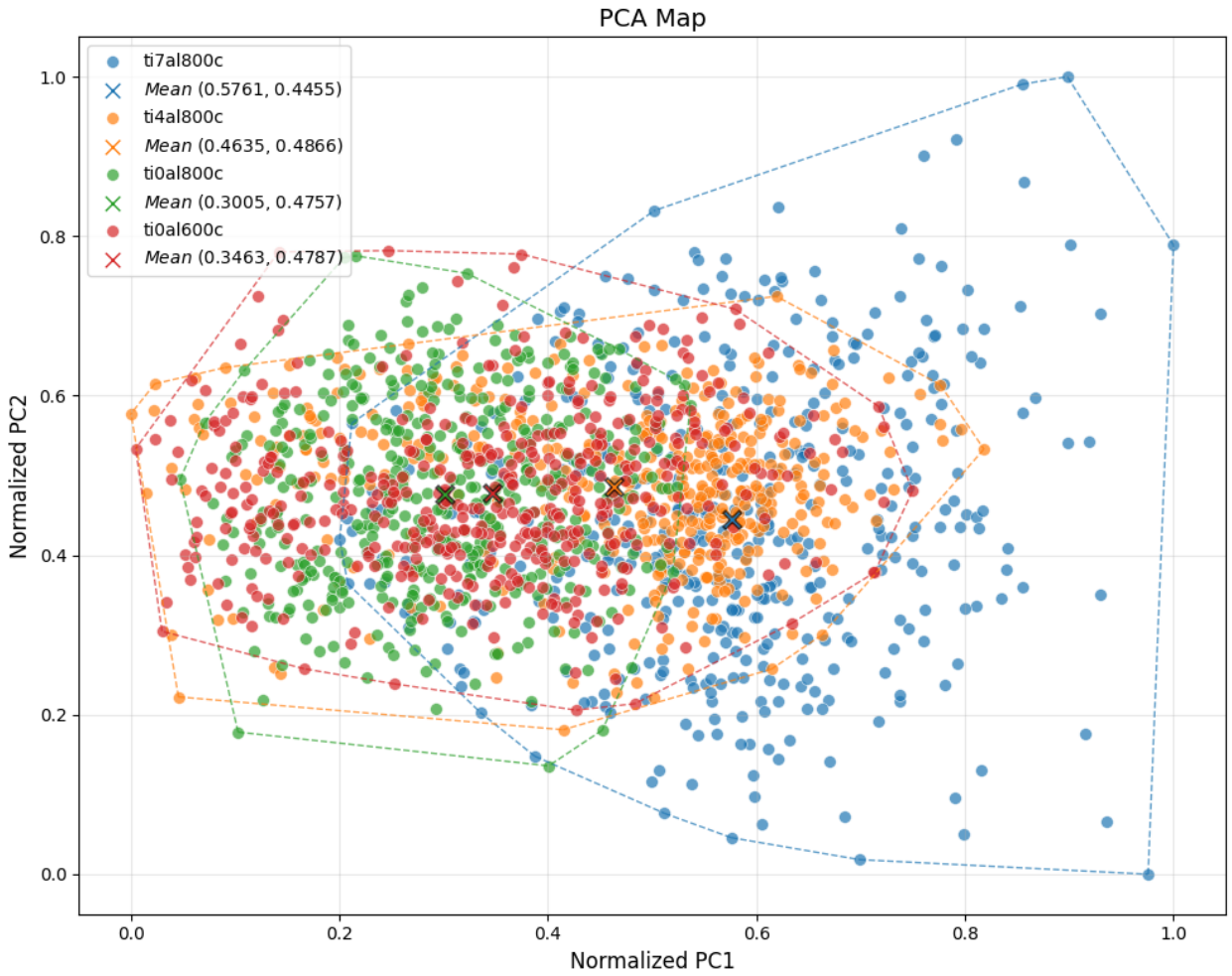

Figure 3.10: PCA map for experimental Titanium-Aluminum microstructures (color images)

When the same image is analyzed using the Red-Green-Blue (RGB) channel values, the

Table 3.8: PCA (Color) statistical analysis for the experimental data of Titanium-Aluminum alloys

	Max Variation		STD Deviation	
Group	PC1	PC2	PC1	PC2
Ti7Al at 800 °C	0.4622	0.5122	0.1636	0.1604
Ti4Al at 800 °C	0.4215	0.3338	0.1586	0.0953
Ti0Al at 800 °C	0.3385	0.3621	0.1148	0.0959
Ti0Al at 600 °C	0.4189	0.3508	0.1760	0.1056

PCA map is slightly different compared to the grayscale mode. The average PC value of "ti0al800C" is closer to "ti0al600C" rather than "ti4al800C", as shown in Fig. 3.10. This difference can potentially relate to the different intensity of the three color channels between each group. In this case, the color variances for these two groups are similar; they can have similar amounts of red, green, and blue channel values in the image. Since different colors of an EBSD microstructure image represent different crystallographic orientations of the grains, this result can potentially imply that the Ti-0Al alloy under 800°C treatment has more similar crystallographic orientations to Ti-0Al under 600 °C than Ti-4Al under 800 °C. With the inclusion of RGB values, there are three channels instead of one, and thus the expected explained variance is lower compared to the grayscale input since more dimensions are added to the analysis. In this case, it has explained variances of 2.85 percent for PC1 and 1.22 percent for PC2, and the number of components to describe 95 percent of the variance in this case is found to be 872, with a dimension of 7,500 for each image.

Moving on to the synthetic microstructure group as shown in Fig. 3.11 and Fig. 3.12, it has parallel results with the experimental Titanium-Aluminum microstructures. In the grayscale mode shown in Fig. 3.11, synthetic images generated by the DDPM model appear to have PC values that significantly overlap with the experimental group, and they have closer mean values as well. This agrees with the corresponding Hu moment plot, where the average PC

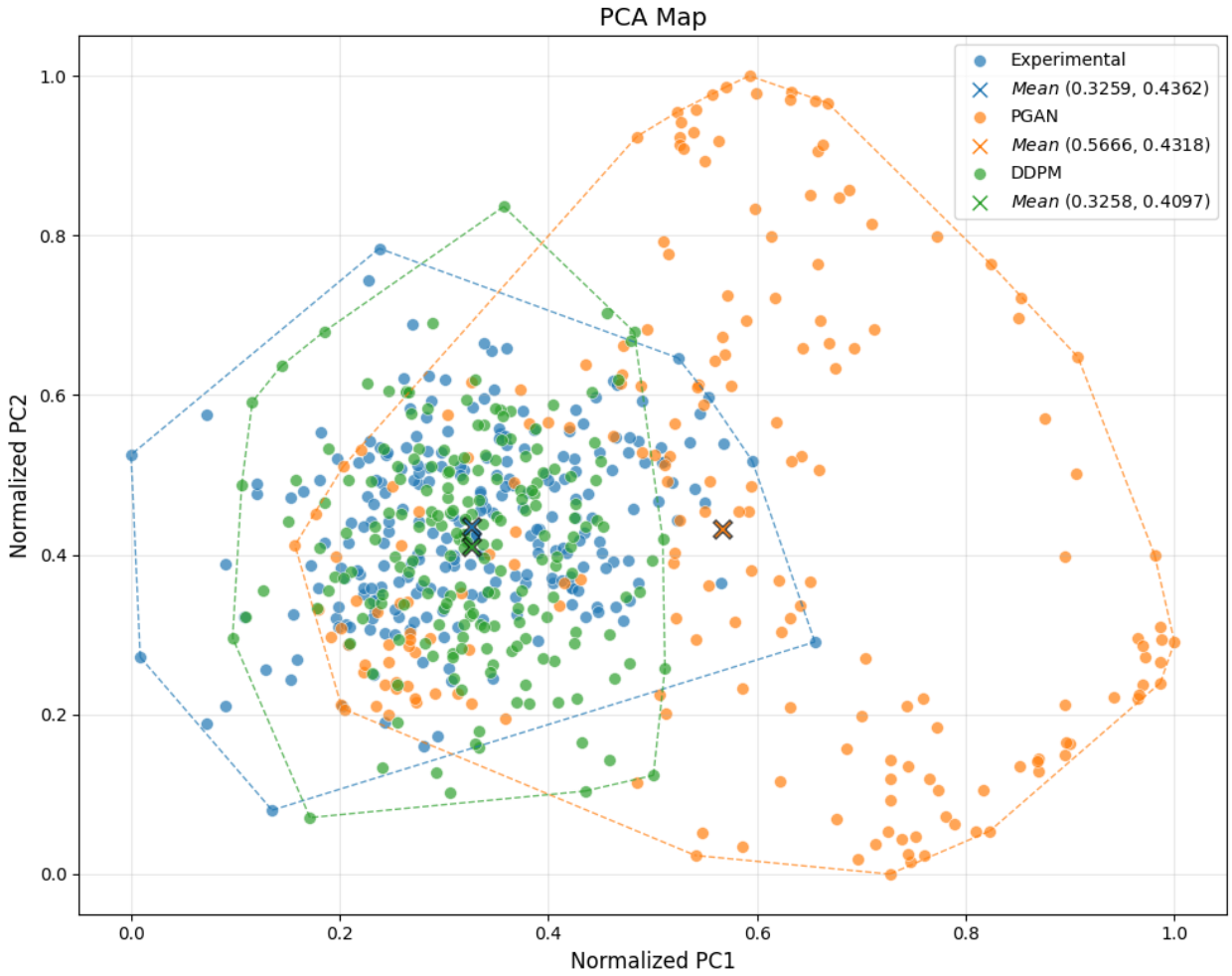

Figure 3.11: PCA map for synthetic Titanium-Aluminum microstructures (grayscale)

value of PGAN is far apart from the other two. However, the consideration of the RGB channels (or color image) brings the cluster of the experimental group away from the DDPM and closer to the PGAN, as the cluster of the experimental group is almost embedded within the PGANs. This result implies that while synthetic microstructure images generated from DDPM might have closer characteristics with the experimental group in grayscale, with the consideration of three color channels, images generated from PGAN contain more pixels that have similar colors to the experimental image. This phenomenon is visible in Fig. 2.2, as the randomly selected Ti-Al image (2.2b) from the PGAN group has a close color tone compared

Table 3.9: PCA (Grayscale) statistical analysis for the synthetic data of Titanium-Aluminum alloys

	Max Variation		STD Deviation	
Group	PC1	PC2	PC1	PC2
Experimental	0.3361	0.3571	0.1097	0.1064
PGAN	0.4418	0.5627	0.2251	0.2687
DDPM	0.2309	0.4179	0.0870	0.1307

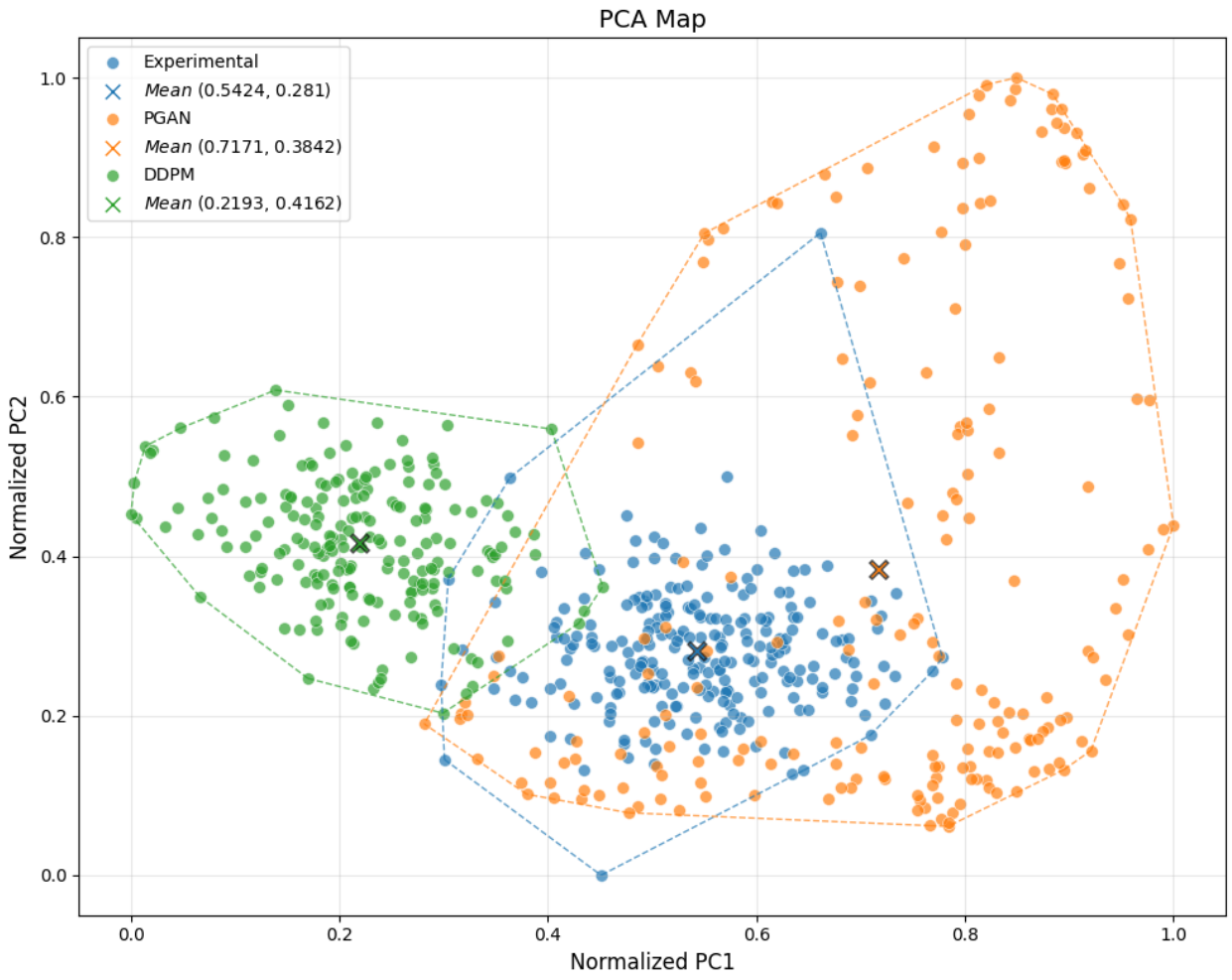

Figure 3.12: PCA map for synthetic Titanium-Aluminum microstructures (color images)

Table 3.10: PCA (Color) statistical analysis for the synthetic data of Titanium-Aluminum alloys

	Max Variation		STD Deviation	
Group	PC1	PC2	PC1	PC2
Experimental	0.2399	0.5315	0.0866	0.0827
PGAN	0.4356	0.6396	0.1736	0.3269
DDPM	0.2315	0.2311	0.0863	0.0835

to the experiment image (2.2a).

The explained variance of the two principal components adds up to 12.27 percent for the grayscale mode and 16.58 percent for the color mode, and the numbers of components to explain 95 percent variance are 219 and 298, respectively. Since there are three groups in total this time, the data is less complex. Therefore, the explained variances are larger than the PCA with four groups. Moreover, the PGAN cluster appears to have larger spreads on both the PCA map of grayscale and color mode, which implies that the microstructures generated from the PGAN model are not as consistent as the experimental and DDPM microstructures. This can also be seen in Table 3.9 and Table 3.10 that the max variations and standard deviations for PGAN are much larger compared to those from the other two groups.

Table 3.11: PCA (Grayscale) statistical analysis with different window sizes

	Max Variation		STD Deviation	
Group	PC1	PC2	PC1	PC2
400x400	0.5782	0.5309	0.2207	0.1937
500x500	0.5594	0.4665	0.2080	0.1883
600x600	0.5197	0.4136	0.1948	0.1770
700x700	0.4787	0.4054	0.1865	0.1751
800x800	0.4469	0.4276	0.1780	0.1727
900x900	0.4129	0.4341	0.1695	0.1751

For the window size investigation using the Inconel-718 microstructure image, both grayscale

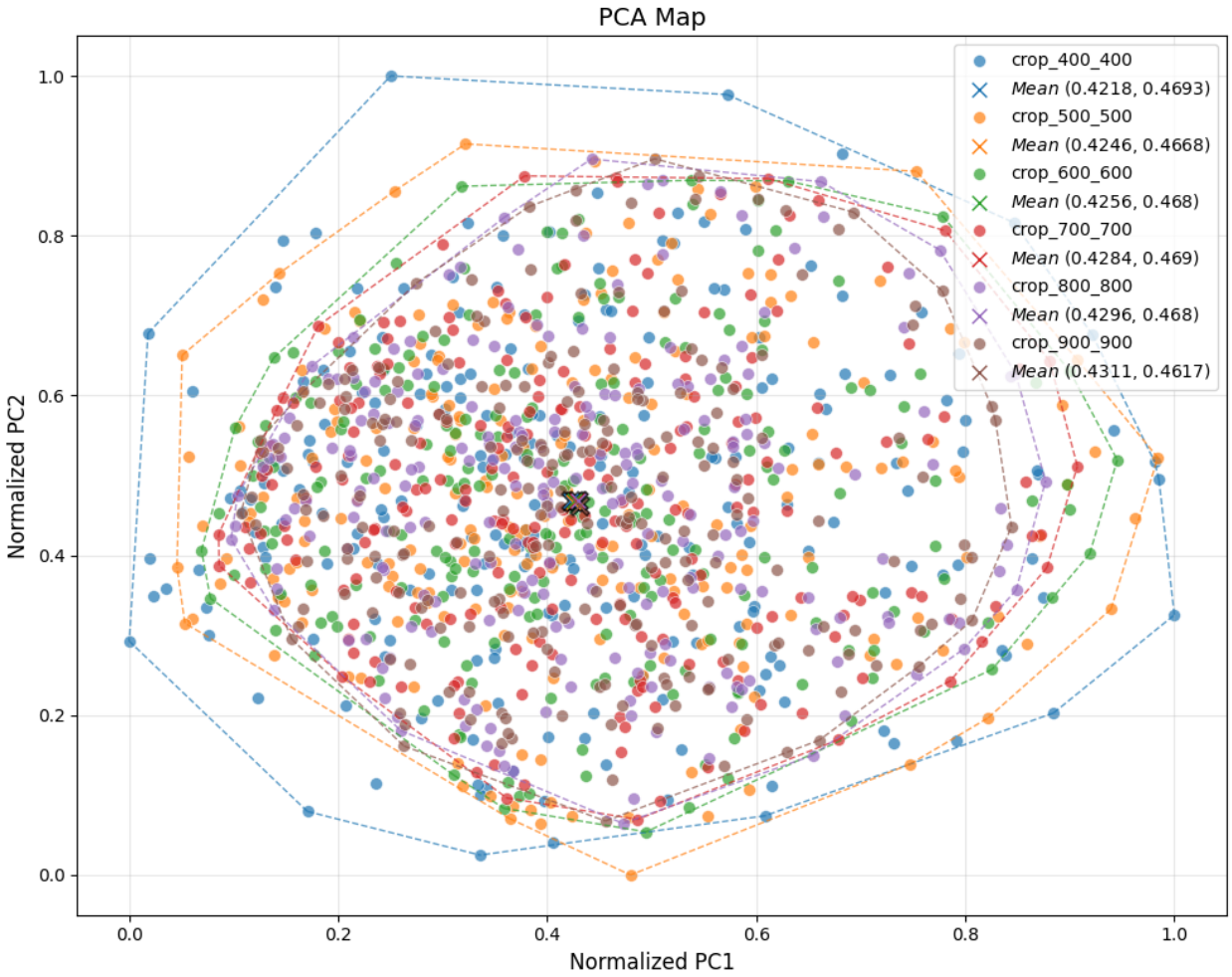

Figure 3.13: PCA map for Inconel-718 microstructures (grayscale)

Table 3.12: PCA (Color) statistical analysis with different window sizes

	Max Variation		STD Deviation	
Group	PC1	PC2	PC1	PC2
400x400	0.5121	0.4822	0.2000	0.1939
500x500	0.4943	0.5054	0.1870	0.1897
600x600	0.4410	0.4776	0.1757	0.1803
700x700	0.3983	0.4916	0.1683	0.1743
800x800	0.3592	0.4540	0.1615	0.1659
900x900	0.3281	0.3964	0.1547	0.1589

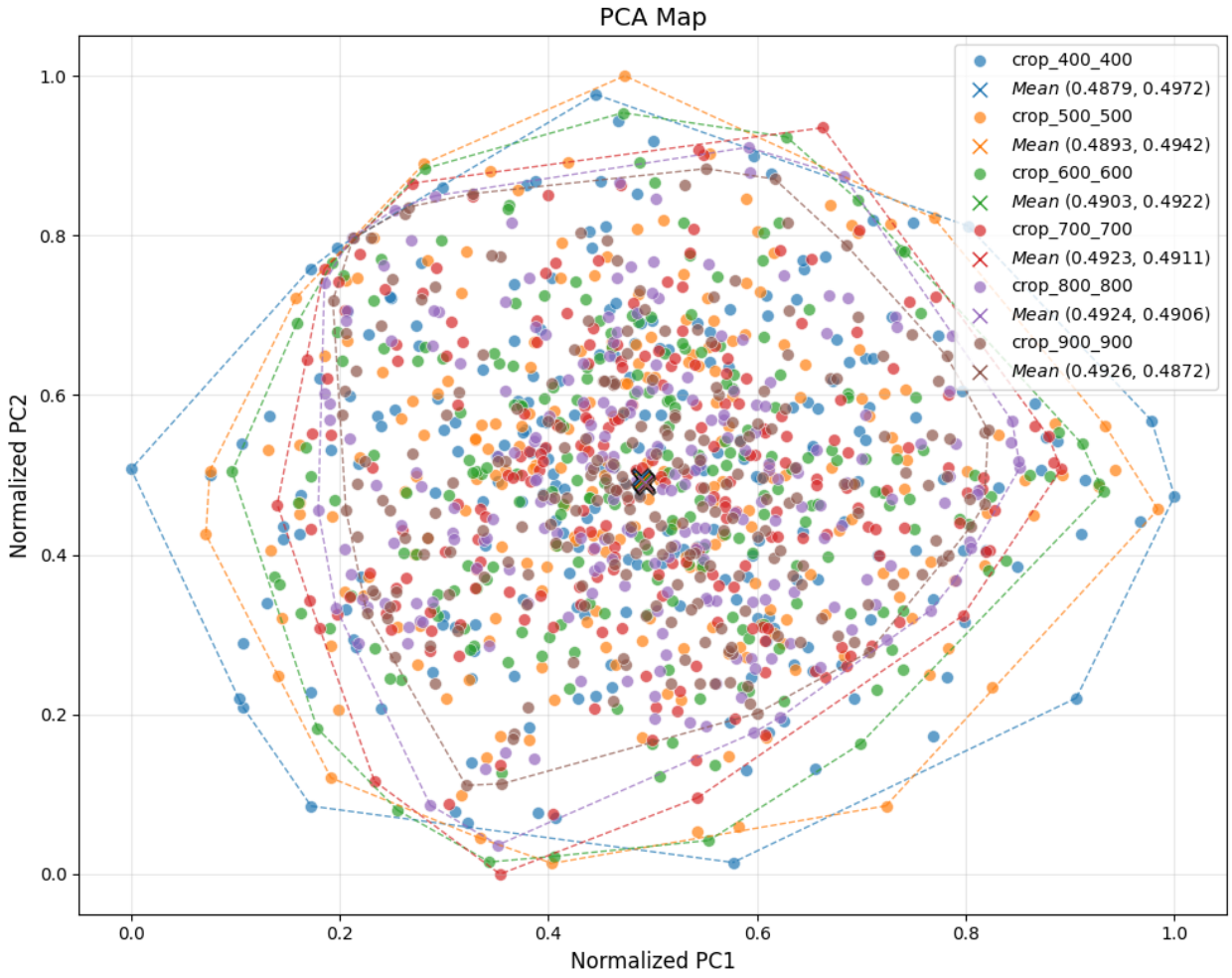

Figure 3.14: PCA map for Inconel-718 microstructures (color images)

(Fig. 3.13) and color mode (Fig. 3.14) PCA demonstrate close patterns. The average PC values for all window sizes are centered and overlapped with each other since images from different groups are all cropped from a single Inconel-718 microstructure image. As a result, the explained variances are found to be higher, with 29.9 percent for grayscale and 10.98 percent for the color mode. The number of components to explain 95 percent variance is found to be 223 for grayscale PCA and 494 for color PCA. The areas of convex hulls, or the spreads of the PC value, become smaller as the window size becomes larger, which is shown in Table 3.11 and Table 3.12 that the standard deviations tend to decrease. This can

also be observed from the corresponding Hu moment plot. However, different from the Hu moments, which capture the shapes and sizes of the grain, PCA focuses on the variations of the data.

3.2.2 Results for Unit Cells and Spinodoids

Figure 3.15 presents a PCA map for unit cell and spinodoid metamaterials. Each data point is represented by the corresponding material image, enabling direct visual interpretation. From the plot, unit cells tend to form tighter clusters since all of them stack on top of each other around the position (0.19, 0.5) in the left and central regions of the PCA map. This is a direct result of the periodic and geometrically consistent characteristics of the unit cell topologies. In contrast, spinodoids, characterized by their non-periodic, smoothly varying topologies, are spread more broadly across the map. This distribution reflects the inherent structural diversity and randomness introduced by their Gaussian Random Field (GRF)-based generation process.

However, an important limitation of PCA is highlighted in this result: PCA is not invariant to rotation. As a result, spinodoids having the same topological features but different orientations are mapped to different regions on the PCA map, which can be observed from the plot. On the other hand, Hu moments and PEMs are mathematically designed to be invariant to rotation, scale, and translation. Therefore, they produce consistent values even when the material image is rotated, offering a more reliable metric when rotational consistency is desired.

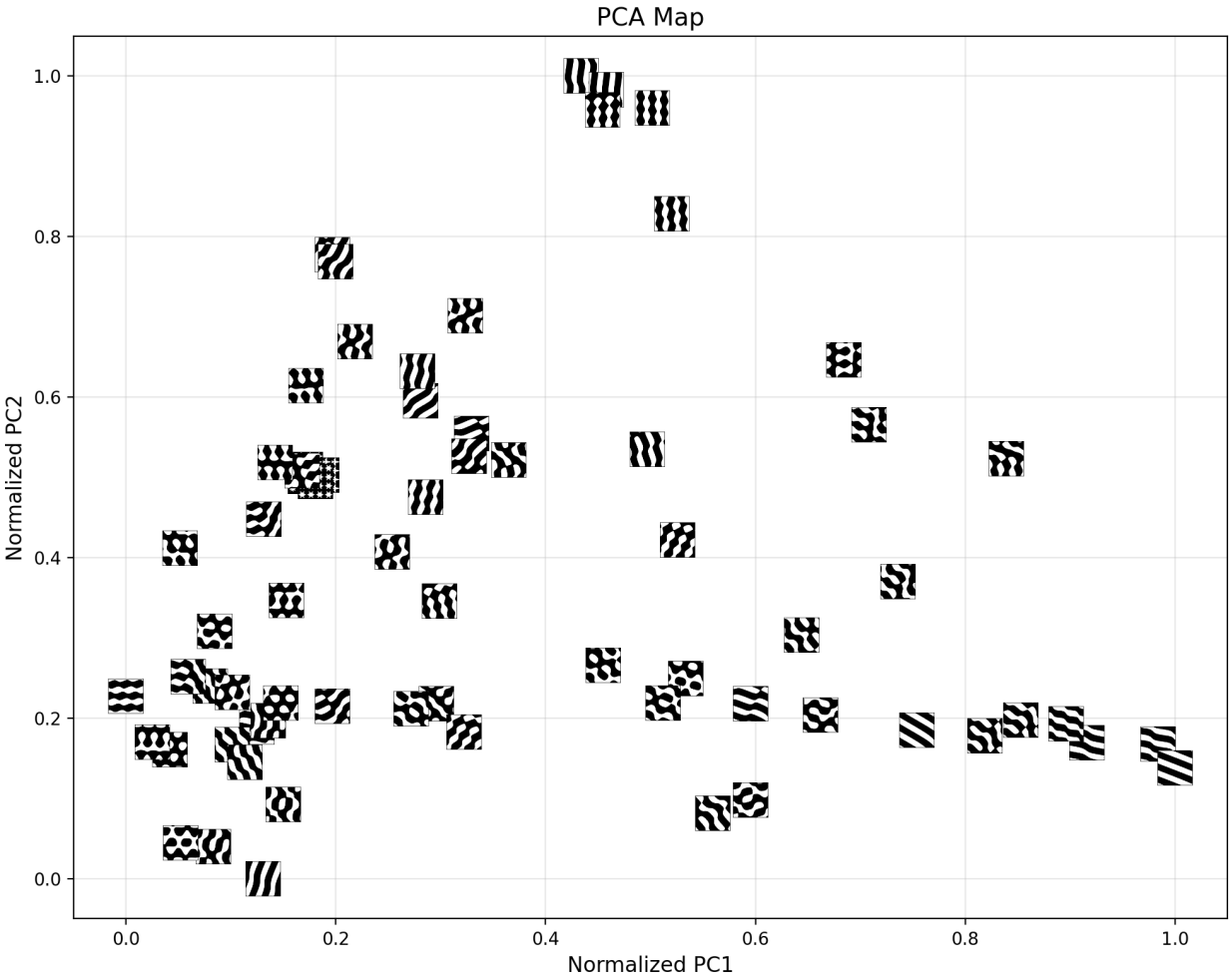

Figure 3.15: PCA map for spinodoid topologies

Chapter 4

Conclusions

In this dissertation, three comprehensive data-driven methods for quantifying the shape, grain morphology, and structural topology of engineering materials are presented. These methods include the Hu moments, which are invariant to rotation, scaling, and translation of shapes, Principal Eigenvalue Moment (PEM), which integrates the first and second Hu moments and represents the shape complexity accurately; and Principal Component Analysis (PCA), a method of reducing the number of dimensions in a data set which identifies the strongest patterns of variation among the distributions of pixel intensities across images. The set of data utilized in the research includes the Titanium-Aluminum alloy microstructures, Inconel 718 superalloy microstructures, mechanical metamaterials with unit cell and spinodoid topologies, as well as synthetic microstructures produced through deep learning algorithms.

The result shows that Hu moments and PEM are reliable to characterize microstructural shape and topology. In particular, the first and second Hu moments precisely encapsulate the differences in grain size and shape asymmetry as well as ellipticity for multiple alloy compositions and processing conditions. Moreover, PEM provides a condensed form of shape features and demonstrates success in microstructural clustering. This can be seen from the results of experimental Ti-Al alloy analysis presented in Section 3.1.1, where the Ti-7Al samples demonstrate a separated cluster and lower Hu moments, indicating larger and circular grains resulting from longer annealing duration.

The PCA results are partially consistent with the patterns observed in Hu moments and PEM analysis. For example, when using grayscale images, the mean for Ti-4Al at 800°C is closer to Ti-0Al at 800°C across all three methods. However, when the color information is taken into account, which is unique in PCA for its ability to map a higher-dimensional data into 2-D data, the result changes as presented in Section 3.2. This distinction becomes more noticeable in the comparison between experimental and synthetic microstructures, where PGAN-generated images appears more similar to experimental samples in terms of color, while DDPM-produced images align more closely with grayscale-based PCA, Hu moment, and PEM results. On the other hand, the PCA results are found to be sensitive to image rotation, which leads to variance when similar microstructures are oriented differently. This limitation is especially apparent in the analysis of unit cells and spinodoid topologies, where spinodoids with similar topologies but rotated orientations are mapped to different regions on the PCA map.

The effects of different window sizes are explored for synthetic microstructure data. The a larger window size is found to lead to a lower variance in Hu moments and PEM values. This is due to the reduction in structural variations when more overlapping pixels are included in a larger window size. The same outcome can be extracted in PCA maps, where larger window sizes lead to tighter clustering and increased explained variance.

4.1 Limitations

While the proposed approaches present promising results to quantify different grain morphology and structural topology features, the methods are also found to possess some limitations, such as the reliance on 2-D image projections. Although these projections simplify some analyses, 2-D projections do not represent the full complexity of a 3-D microstructural geometry.

The image pre-processing steps are performed, including converting the images to grayscale, cutting out sections, and aligning the images to a common resolution. These steps affect the computed metrics to some extent. In addition, the limited number of materials investigated in this study may not be representative of the broader, more complex material systems (e.g., additively manufactured metallic microstructures) that possess a greater range of complex microstructural features.

4.2 Future works

The future work may concentrate on the previously discussed limitations by expanding the framework to 3-D microstructure datasets obtained through processes such as X-ray computed tomography (CT) [7, 18] or focused ion beam scanning electron microscopy (FIB-SEM) [14, 15, 34] to achieve detailed shape characterization. Other or additional quantification methods, such as Zernike moments[22], Fourier descriptors [37], and topological data analysis (TDA) [33], could produce more sensitive results to structural variances. Including datasets with time-evolving microstructures would enable the framework to capture dynamic changes resulting from thermal and mechanical treatments, expanding its capabilities. Last but not least, the incorporation of the developed quantification pipeline into machine learning models could facilitate automatic classification, clustering, and property prediction, augmenting the application of image-based metrics within computational materials design and informatics.

4.3 Concluding Remarks

Overall, this study highlights the effectiveness of merging invariant geometric descriptors with dimensionality reduction approaches for measuring microstructural shape and topol-

ogy. The methods developed in this study provide a framework that is reproducible and scalable for the analysis of different systems, and which extends the capabilities of materials informatics in the design and optimization processes of sophisticated engineering materials.

Bibliography

[1] Finding and Using Health Statistics, . URL https://www.nlm.nih.gov/oet/ed/stats/02-900.html.

[2] Manual grain counting method: (a) original SEM image of sample 1, (b)..., . URL https://www.researchgate.net/figure/Manual-grain-counting-method-a-original-SEM-image-of-sample-1-b-measuring-by_fig1_354381582.

[3] Hervé Abdi and Lynne J. Williams. Principal component analysis. *WIREs Computational Statistics*, 2(4):433–459, 2010. ISSN 1939-0068. doi: 10.1002/wics.101. URL https://onlinelibrary.wiley.com/doi/abs/10.1002/wics.101. _eprint: https://onlinelibrary.wiley.com/doi/pdf/10.1002/wics.101.

[4] Enes Akca and Ali Gürsel. A Review on Superalloys and IN718 Nickel-Based INCONEL Superalloy. *Periodicals of Engineering and Natural Sciences (PEN)*, 3(1), June 2015. ISSN 2303-4521. doi: 10.21533/pen.v3i1.43. URL http://pen.ius.edu.ba/index.php/pen/article/view/43.

[5] John Allison and Anna Trump. The influence of aluminum content and annealing temperature on static recrystallization in -titanium alloys. URL https://materialscommons.miserver.it.umich.edu/docs/docs/docs/docs/getting-started.

[6] Andrew Campbell, Paul Murray, Evgenia Yakushina, Stephen Marshall, and William Ion. New methods for automatic quantification of microstructural features using digital image processing. *Materials & Design*, 141:395–406, March 2018. ISSN 0264-1275.

doi: 10.1016/j.matdes.2017.12.049. URL https://www.sciencedirect.com/science/article/pii/S0264127517311620.

[7] Ibrahim Fatih Cengiz, Joaquim Miguel Oliveira, and Rui L. Reis. Micro-CT – a digital 3D microstructural voyage into scaffolds: a systematic review of the reported methods and results. *Biomaterials Research*, 22(1):26, September 2018. doi: 10.1186/s40824-018-0136-8. URL https://spj.science.org/doi/full/10.1186/s40824-018-0136-8. Publisher: American Association for the Advancement of Science.

[8] Abhik Choudhury, Yuksel C. Yabansu, Surya R. Kalidindi, and Anne Dennstedt. Quantification and classification of microstructures in ternary eutectic alloys using 2-point spatial correlations and principal component analyses. *Acta Materialia*, 110: 131–141, May 2016. ISSN 1359-6454. doi: 10.1016/j.actamat.2016.03.010. URL https://www.sciencedirect.com/science/article/pii/S1359645416301604.

[9] Jingjie Dai, Jiyun Zhu, Chuanzhong Chen, and Fei Weng. High temperature oxidation behavior and research status of modifications on improving high temperature oxidation resistance of titanium alloys and titanium aluminides: A review. *Journal of Alloys and Compounds*, 685:784–798, November 2016. ISSN 0925-8388. doi: 10.1016/j.jallcom.2016.06.212. URL https://www.sciencedirect.com/science/article/pii/S0925838816319351.

[10] Dionis Diez and James DeRose. How to Adapt Grain Size Analysis of Metallic Alloys to Your Needs. July 2019. URL https://www.leica-microsystems.com/science-lab/industrial/how-to-adapt-grain-size-analysis-of-metallic-alloys-to-your-needs/.

[11] Zekeriya Ender Eger, Waris Khan, Kuang Kuang, Veera Sundararaghavan, and Pinar

Acar. Comparative Analysis of Synthetic Microstructure Reconstruction for Metallic Aerospace Alloys With Generative Networks. In *AIAA SCITECH 2025 Forum*. American Institute of Aeronautics and Astronautics, January 2025. doi: 10.2514/6.2025-0634. URL https://arc.aiaa.org/doi/abs/10.2514/6.2025-0634. _eprint: https://arc.aiaa.org/doi/pdf/10.2514/6.2025-0634.

[12] David T. Fullwood, Stephen R. Niezgoda, Brent L. Adams, and Surya R. Kalidindi. Microstructure sensitive design for performance optimization. *Progress in Materials Science*, 55(6):477–562, August 2010. ISSN 0079-6425. doi: 10.1016/j.pmatsci.2009.08.002. URL https://www.sciencedirect.com/science/article/pii/S0079642509000760.

[13] Rafael C. Gonzalez, Richard E. Woods, and Barry R. Masters. Digital Image Processing, Third Edition. *Journal of Biomedical Optics*, 14(2):029901, 2009. ISSN 10833668. doi: 10.1117/1.3115362. URL http://biomedicaloptics.spiedigitallibrary.org/article.aspx?doi=10.1117/1.3115362.

[14] M. A. Groeber, B. K. Haley, M. D. Uchic, D. M. Dimiduk, and S. Ghosh. 3D reconstruction and characterization of polycrystalline microstructures using a FIB–SEM system. *Materials Characterization*, 57(4):259–273, December 2006. ISSN 1044-5803. doi: 10.1016/j.matchar.2006.01.019. URL https://www.sciencedirect.com/science/article/pii/S1044580306000623.

[15] Lixin Gu, Nian Wang, Xu Tang, and H. G. Changela. Application of FIB-SEM Techniques for the Advanced Characterization of Earth and Planetary Materials. *Scanning*, 2020(1):8406917, 2020. ISSN 1932-8745. doi: 10.1155/2020/8406917. URL https://onlinelibrary.wiley.com/doi/abs/10.1155/2020/8406917. _eprint: https://onlinelibrary.wiley.com/doi/pdf/10.1155/2020/8406917.

[16] Ming-Kuei Hu. "Visual Pattern Recognition by Moment Invariants". *IRE Transac-*

tions on Information Theory, 8(2):179–187, February 1962. ISSN 2168-2712. doi: 10.1109/TIT.1962.1057692. URL https://ieeexplore.ieee.org/abstract/document/1057692/authors.

[17] Stinville J.C., Hestroffer J.M., and Charpagne M.A. Multi-modal dataset of a polycrystalline metallic material: 3D microstructure and deformation fields, July 2022. URL https://datadryad.org/dataset/doi:10.5061/dryad.83bk3j9sj.

[18] Yebin Jiang, Jenny Zhao, Er-Yuan Liao, Ru-Chun Dai, Xian-Ping Wu, and Harry K. Genant. Application of micro-ct assessment of 3-d bone microstructure in preclinical and clinical studies. *Journal of Bone and Mineral Metabolism*, 23(1):122–131, January 2005. ISSN 1435-5604. doi: 10.1007/BF03026336. URL https://doi.org/10.1007/BF03026336.

[19] William D. Callister Jr and David G. Rethwisch. *Materials Science and Engineering: An Introduction*. John Wiley & Sons, June 2020. ISBN 978-1-119-72177-2. Google-Books-ID: dmoTEQAAQBAJ.

[20] Surya R Kalidindi. Initial Microstructure - an overview | ScienceDirect Topics, 2015. URL https://www.sciencedirect.com/topics/engineering/initial-microstructure.

[21] Surya R. Kalidindi, Stephen R. Niezgoda, and Ayman A. Salem. Microstructure informatics using higher-order statistics and efficient data-mining protocols. *JOM*, 63(4):34–41, April 2011. ISSN 1543-1851. doi: 10.1007/s11837-011-0057-7. URL https://doi.org/10.1007/s11837-011-0057-7.

[22] A. Khotanzad and Y.H. Hong. Invariant image recognition by Zernike moments. *IEEE Transactions on Pattern Analysis and Machine Intelligence*, 12(5):489–497, May

1990. ISSN 1939-3539. doi: 10.1109/34.55109. URL https://ieeexplore.ieee.org/abstract/document/55109.

[23] Marat I. Latypov, Markus Kühbach, Irene J. Beyerlein, Jean-Charles Stinville, Laszlo S. Toth, Tresa M. Pollock, and Surya R. Kalidindi. Application of chord length distributions and principal component analysis for quantification and representation of diverse polycrystalline microstructures. *Materials Characterization*, 145:671–685, November 2018. ISSN 1044-5803. doi: 10.1016/j.matchar.2018.09.020. URL https://www.sciencedirect.com/science/article/pii/S1044580318313743.

[24] Sheng Liu and Pinar Acar. Mapping material-property space of cellular metamaterials under uncertainty. *Computational Materials Science*, 233:112716, January 2024. ISSN 0927-0256. doi: 10.1016/j.commatsci.2023.112716. URL https://www.sciencedirect.com/science/article/pii/S0927025623007103.

[25] Sheng Liu and Pınar Acar. Parameter Space Exploration of Cellular Mechanical Metamaterials Using Genetic Algorithms. *AIAA Journal*, 61(8):3633–3643, 2023. ISSN 0001-1452. doi: 10.2514/1.J062864. URL https://doi.org/10.2514/1.J062864. Publisher: American Institute of Aeronautics and Astronautics _eprint: https://doi.org/10.2514/1.J062864.

[26] Sheng Liu and Pınar Acar. Generative Adversarial Networks for Inverse Design of Two-Dimensional Spinodoid Metamaterials. *AIAA Journal*, 62(7):2433–2442, 2024. ISSN 0001-1452. doi: 10.2514/1.J063697. URL https://doi.org/10.2514/1.J063697. Publisher: American Institute of Aeronautics and Astronautics _eprint: https://doi.org/10.2514/1.J063697.

[27] Stephen R. Niezgoda, Yuksel C. Yabansu, and Surya R. Kalidindi. Understanding and visualizing microstructure and microstructure variance as a stochastic process.

Acta Materialia, 59(16):6387–6400, September 2011. ISSN 1359-6454. doi: 10.1016/j.actamat.2011.06.051. URL https://www.sciencedirect.com/science/article/pii/S1359645411004654.

[28] Karl Pearson. LIII. On lines and planes of closest fit to systems of points in space. *The London, Edinburgh, and Dublin Philosophical Magazine and Journal of Science*, 2(11):559–572, November 1901. ISSN 1941-5982. doi: 10.1080/14786440109462720. URL https://doi.org/10.1080/14786440109462720. Publisher: Taylor & Francis _eprint: https://doi.org/10.1080/14786440109462720.

[29] Zongrui Pei, Kyle A. Rozman, Ömer N. Doğan, Youhai Wen, Nan Gao, Elizabeth A. Holm, Jeffrey A. Hawk, David E. Alman, and Michael C. Gao. Machine-Learning Microstructure for Inverse Material Design. *Advanced Science*, 8(23):2101207, 2021. ISSN 2198-3844. doi: 10.1002/advs.202101207. URL https://onlinelibrary.wiley.com/doi/abs/10.1002/advs.202101207. _eprint: https://onlinelibrary.wiley.com/doi/pdf/10.1002/advs.202101207.

[30] Arulmurugan Senthilnathan, Pınar Acar, and Marc De Graef. Markov Random Field based microstructure reconstruction using the principal image moments. *Materials Characterization*, 178:111281, August 2021. ISSN 1044-5803. doi: 10.1016/j.matchar.2021.111281. URL https://www.sciencedirect.com/science/article/pii/S1044580321004034.

[31] Arulmurugan Senthilnathan, Iman Javaheri, Hengduo Zhao, Veera Sundararaghavan, Marc DeGraef, and Pınar Acar. Uncertainty quantification of metallic microstructures using principal image moments. *Computational Materials Science*, 215:111775, December 2022. ISSN 0927-0256. doi: 10.1016/j.commatsci.2022.111775. URL https://www.sciencedirect.com/science/article/pii/S0927025622004864.

[32] Geology In Team. Grain Size: What is Grain Size and How is It Measured? URL https://www.geologyin.com/2023/06/what-is-sediment-grain-size-how-is-it.html.

[33] Larry Wasserman. Topological Data Analysis. *Annual Review of Statistics and Its Application*, 5(Volume 5, 2018):501–532, March 2018. ISSN 2326-8298, 2326-831X. doi: 10.1146/annurev-statistics-031017-100045. URL https://www.annualreviews.org/content/journals/10.1146/annurev-statistics-031017-100045/. Publisher: Annual Reviews.

[34] C Shan Xu, Kenneth J Hayworth, Zhiyuan Lu, Patricia Grob, Ahmed M Hassan, José G García-Cerdán, Krishna K Niyogi, Eva Nogales, Richard J Weinberg, and Harald F Hess. Enhanced FIB-SEM systems for large-volume 3D imaging. *eLife*, 6:e25916, May 2017. ISSN 2050-084X. doi: 10.7554/eLife.25916. URL https://doi.org/10.7554/eLife.25916. Publisher: eLife Sciences Publications, Ltd.

[35] Chao Xu, Shuming Gao, and Ming Li. A novel PCA-based microstructure descriptor for heterogeneous material design. *Computational Materials Science*, 130:39–49, April 2017. ISSN 0927-0256. doi: 10.1016/j.commatsci.2016.12.031. URL https://www.sciencedirect.com/science/article/pii/S0927025616306589.

[36] Saltuk Yildiz, Zekeriya Ender Eger, and Pinar Acar. Additively Manufactured Spinodal Metamaterials for Aerospace Systems: A Data-Driven Design Framework. In *AIAA SCITECH 2025 Forum*. American Institute of Aeronautics and Astronautics, January 2025. doi: 10.2514/6.2025-1551. URL https://arc.aiaa.org/doi/abs/10.2514/6.2025-1551. _eprint: https://arc.aiaa.org/doi/pdf/10.2514/6.2025-1551.

[37] Dengsheng Zhang and Guojun Lu. Generic Fourier descriptor for shape-based image retrieval. In *Proceedings. IEEE International Conference on Multimedia and Expo*,

volume 1, pages 425–428 vol.1, August 2002. doi: 10.1109/ICME.2002.1035809. URL https://ieeexplore.ieee.org/abstract/document/1035809.